

INCLUSIVE  $K^+K^-$  PRODUCTION IN REACTIONS  $\pi^+p, K^+p$   
AND  $pp$  AT 200 GEV/C

by

VICTOR SUCHOREBROW

B.S., Yale University  
(1978)

SUBMITTED IN PARTIAL FULFILLMENT  
OF THE REQUIREMENTS FOR THE  
DEGREE OF

DOCTOR OF PHILOSOPHY

at the

MASSACHUSETTS INSTITUTE OF TECHNOLOGY

February 22, 1985

Signature of Author. . . . . Department of Physics, 1985

Certified by . . . . . Thesis Supervisor

Accepted by. . . . . Chairman, Departmental Committee

INCLUSIVE  $K^+K^-$  PRODUCTION IN REACTIONS  $\pi^+p$ ,  $K^+p$   
AND  $pp$  AT 200 GEV/C

by

VICTOR SUCHOREBROW

Submitted to the Department of Physics  
on February 22, 1985 in partial fulfillment of the requirements  
for the Degree of Doctor of Philosophy

ABSTRACT

Preliminary results are presented from 4000  $\pi^+p$ ,  $K^+p$  and  $pp$  events at 200 GeV/c using the Fermi Lab Hybrid spectrometer. A study of strange particle production in the central region of  $0.0 < x_F < 0.3$  reveals a strong correlation in rapidity between a  $K^+$  and  $K^-$  produced in coincidence.

The calibration and performance of CRISIS, a particle identifier which uses multiple ionization sampling in an argon-CO<sub>2</sub> filled drift chamber, is described in detail. As a check of its performance, two common resonances,  $pp \rightarrow \Delta^{++} + X$  and  $K^+p \rightarrow K^{*0}(890) + X$ , are studied. The total cross sections obtained are  $5.7 \pm 1.6$  mb and  $5.3 \pm 1.9$  mb respectively. A  $\phi$  signal is also observed.

The results are in good agreement with the Lund Model which, although designed originally for quark jets, is expected to give reasonable results for low- $p_T$  hadron-hadron interactions. The data, however, seems to indicate a stronger short range correlation in strangeness than predicted by the model.

Thesis Supervisor: Robert I. Hulsizer

Title: Professor of Physics

## I INTRODUCTION

The idea of a quark structure of hadrons, first proposed by Gell-Mann<sup>1</sup> and Zweig<sup>2</sup> in 1964, has seen a lot of success in the last two decades. Since that time the model has been developed into a precise theory known as Quantum Chromodynamics (QCD). Many physicists today believe that QCD will be a likely candidate for the correct theory of strong interactions and that, in the near future, it will be combined with a similar gauge theory for electroweak interactions to produce a grand unified theory (GUT) of elementary particle physics.

There are, however, still some serious problems in applying QCD to a large amount of experimental data. In particular, the difficulty in predicting the static properties of hadrons, their formation and processes in which they interact "softly" (without large momentum transfer), is a serious problem. In QCD, one can express the sum of certain contributions to the scattering amplitude as a Born term with a "running" coupling constant  $\alpha(Q^2)$  which depends on the momentum transfer squared  $Q^2$ . In strong interactions, unfortunately,  $\alpha$  is large at low  $Q^2$ . Only at high  $Q^2$  do gluon-gluon interactions result in a decrease of  $\alpha$ . This effect, called "asymptotic freedom", restricts the application of perturbative theory in QCD to large  $Q^2$  problems. Thus, in order to describe the phenomenology of "soft" or low  $p_T$  processes, one has to use simplified models. Their successes or failures will, it is hoped, provide clues for QCD as to the strategies

that should be applied to give meaningful answers to a wide range of phenomenological questions.

During the past few years, studies of low- $p_T$  hadronic collisions have changed their focus of interest from single-particle inclusive production to resonance inclusive production and multiparticle inclusive production. Single-particle studies have a disadvantage from the fact that it is hard to distinguish between direct production and intermediate production through the decay of resonances or particles, such as the  $K^*$ ,  $\rho$ ,  $\Lambda$ ,  $\phi$  or  $\Delta$ . The competing models like the quark-recombination, quark-counting, quark-fragmentation or perturbative QCD approach describe successfully a large number of single-particle inclusive processes. However, there have been few studies done on multiparticle inclusive production in the central region at FNAL and ISR energies. The main reasons are:

- 1) theory is at its weakest in predicting accurate quantitative results in this region;
- 2) the number of complex processes involved in such reactions makes it difficult experimentally to pick out primary particle production;
- 3) the difficulty in separating centrally produced particles from those that are a product of the beam or target diffraction.

The present work attempts such a study. Preliminary results on 1442  $\pi^+p$ , 670  $K^+p$ , and 1774  $pp$  events at 200 GeV/c are presented. The data were taken during the spring of 1982 run of experiment E565/570 at the Fermi National Accelerator

Laboratory using the 30" bubble chamber and the downstream Fermilab Hybrid Spectrometer (FHS). The aim of the present study is to use the particle identifier CRISIS to select strange particle production in the central region (the region sensitive to CRISIS). In particular,  $\pi^+p$  and  $pp$  events with topologies of four or greater were selected (to insure no initial strange valence quarks) and those that had an identified  $K^+$  and  $K^-$  studied.

## II EXPERIMENT

### A) Beam

The data presented are a result of experiment E565/570 performed at the Fermi National Accelerator Laboratory in the Neutrino secondary beam line during the spring of 1982. The FHS was provided with positive and negative beams of pions, kaons and protons at a momentum of 200 GeV/c. In addition, several other beam energies and intensities were available for calibration purposes. All the detectors of the FHS were designed to be compatible with the bubble chamber expansion cycle which was typically around 1.3 ms. An average of 6-7 beam particles per expansion was maintained, resulting in approximately one event for every four bubble chamber pictures (a higher beam intensity would have considerably reduced the efficiency of subsequent data analysis). For this purpose, during each main accelerator cycle ( $\sim 10$  s) an upstream pulsed magnet transferred several slow-spill (ping) slices into the N7 line of the FHS. The number of particles reaching the bubble chamber was further reduced to about 7 by a "kicker" magnet.

Since the secondary 200 GeV positive beam (which is extracted from the primary 400 GeV beam of the accelerator) contained about 96% protons, a 15 foot polyethylene filter was inserted in the beamline. The result was to improve the  $\pi^+/p$  and  $K^+/p$  ratios, giving a typical beam composition of  $\pi^+$ ,  $K^+$ ,  $p \sim 50\%$ ,  $15\%$ ,  $35\%$ . The final beam was shaped from its original

circular form to match the rectangular cross section of the bubble chamber (i.e., compressed in the horizontal direction and stretched in the vertical) by a quadrupole magnet. Finally, two smaller magnets served to fine tune the position of the beam at the bubble chamber.

#### B) Upstream detectors

Three proportional wire chamber (PWC) triplets located approximately 180, 16 and 2.5 meters upstream of the bubble chamber served three main purposes:

- 1) focus and position the beam;
- 2) properly identify each beam particle and match it to the corresponding track in the bubble chamber picture;
- 3) define the beam axis for the event.

The triplets contained three planes of wires positioned  $120^\circ$  relative to each other. Each plane consisted of 48 wires with 2 millimeter spacing. Hits in the chambers were picked up by the closest wire which sent the signal through a discriminator, amplified it and stored it in a 16-bit local memory channel. Each bit of the memory would correspond to a master gate triggered by the incident beam. The efficiency of every upstream PWC plane was better than 96%. This was established by mounting the planes on a movable stand and using a cesium-137 radioactive source to send electrons through the chamber. Two small scintillators, one in front and the other in the back of the PWC plane were used to open the gate for the electronics and detect the electrons leaving the chamber respectively.

To complete the upstream system, three Cerenkov detectors were used to identify the individual beam particles.

C) Downstream spectrometer

The 30 inch Hydrogen Bubble Chamber served as both a target and an optical detector. Besides providing a source of protons from the hydrogen nuclei, the chamber contained several metal foils within its volume. Located near the entrance window, foils of gold, silver and magnesium were provided for the study of hadron-nuclei interactions (experiment 565), while the hadron-proton interactions in the liquid hydrogen constituted experiment 570. The chamber was enclosed in an electromagnet whose current of 11.8 kiloamperes provided a 20 kilogauss magnetic field which was approximately cylindrically symmetric throughout the inner volume of the chamber. Four camera ports contained three regular cameras and one special high resolution camera<sup>3</sup>. The latter was to provide a high resolution study of short decays and/or interactions not observable with the other cameras. This was at the expense of a rather limited depth of field of a couple of centimeters. During each ping (bubble chamber expansion), flashes were triggered and pictures taken. The flash for the high resolution camera came earlier since its greater magnification could resolve smaller bubbles which grow in time. Eleven fiducials were etched on each of the two windows of the chamber to provide an eventual three-dimensional reconstruction of the entire event. Typically, six expansions during the 1 second

slow-spill were achieved for every 10-15 second main accelerator cycle.

Figure 1 shows the Fermilab Hybrid Spectrometer set-up. To improve the momentum resolution of the faster secondaries, seven large (1 m x 1 m) proportional wire chambers and three drift chamber triplets were installed. The PWCs use the same amplifiers and readout electronics as do the upstream triplets and have a similar 2 millimeter wire spacing. Two of these planes were fixed on the exit face of the bubble chamber magnet and offset by 1 millimeter for better precision. The remaining five PWC planes made up a triplet with wires oriented at an angle of  $120^\circ$  relative to one another. The two extra planes, offset by 1 millimeter, were included to improve the resolution.

Three drift chambers (1.2 m x 1.2 m) each containing three sense planes arranged as a  $120^\circ$  triplet were inserted further downstream (one between the last PWC and CRISIS and two between CRISIS and the forward gamma detector). Since, in addition to detecting wire hits, a precise measurement of the drift time is required (1 inch being the maximum drift distance), a separate set of electronics with its own micro-processor is used to control the acquisition of data and later pass it on to the main computer for permanent storage.

The CRISIS detector, used to identify fast secondaries, was inserted 5 meters behind the bubble chamber. Having an active cross section of 1 m x 1 m, it works on a similar principle as a drift chamber with the important feature of

being able to accurately measure and store the ionization produced in the gas by a charged particle passing through it. It was designed to separate  $\pi$ , K and p's in the range of 5-100 GeV. The details of its construction and performance will be described in a later section.

A Forward Gamma Detector<sup>4</sup>, placed 9 feet downstream from the bubble chamber, was constructed for the purpose of measuring positions and energies of high-energy photons. The major features were:

- 1) a converter whose four radiation lengths of lead glass initiated the shower;
- 2) three planes of plastic scintillators (190 total) reconstructed the center of the shower;
- 3) twenty-five large blocks of lead glass acted as an absorber for energy measurements.

Finally, at the end of the FHS, a muon detector was used to distinguish the hadron beams (which didn't interact in the bubble chamber) from muons. This consisted of a scintillator followed by six feet of iron, ten feet of concrete and another scintillator.

The data acquisition of the entire system was controlled by a PDP-11/45 computer. An incident beam triggered the master gate which enabled all the detectors. The signals in the channels receiving a hit were amplified, digitized and then stored temporarily into local memory (different for every detector). After the data had been accumulated, the PWC, DC and CRISIS each had their own microprocessor which scanned the

memory and transferred it to the PDP11 via a CAMAC (Computer Automated Measurement and Control) Dataway for permanent storage.

The on-line data processing was done by the Fermilab RTMULTI software package modified by Steiner and Taft<sup>5</sup> for E565/570. During the data-taking period (slow spill), the data acquisition part of the program (RTDA) stored the information in the detectors' local memory through the CAMAC Dataway. The rest of the time the data analysis part, called MULTI, performed various useful tasks such as producing graphs and making periodic calibrations of the FGD and CRISIS detectors.

### III PARTICLE IDENTIFICATION

#### A) Conventional Techniques

Particle identification is one of the major goals for high-energy physicists. In practice, however, it is also a very difficult task to accomplish especially for particles in the relativistic range of  $\beta\gamma \geq 5$ . The inability to identify secondaries greatly prohibits a complete analysis of an interaction: production and exchange of quantum numbers cannot be studied, Lorentz invariant quantities cannot be constructed and the analysis can only be performed in terms of laboratory variables.

Leptons are somewhat easier to detect. Muons, which are not too different in mass from the pions, can be identified by their ability to penetrate a large amount of matter without interacting strongly. Electrons, because of their very small mass, can be identified by their ability to initiate electromagnetic showers in high-Z materials. Hadrons, on the other hand, must be identified by their mass. In particular, since we can measure a charged particle's momentum  $p$  in a magnetic field, from the relation  $\beta\gamma = p/mc$ , a precise measurement of  $\beta$  will give the particle's mass.

Two conventional methods, widely used today to identify particles, become inefficient or impractical in identifying secondaries in the high relativistic range. The first is the time of flight method which measures the time a particle takes in traversing a distance  $s$ . For example, at a given momentum  $p$ , the difference in time between two particles of mass  $m_1$

and  $m_2$  is  $t_1 - t_2 \sim (s/4c) (m_1^2 - m_2^2) c^2 / p^2$ . Assuming a time resolution of a fraction of a nanosecond, a path length of roughly  $p^2$  meters is required to separate pions from kaons at a momentum  $p$  GeV/c. This method is clearly impractical when the momentum exceeds a few GeV.

A more common technique used to identify particles takes advantage of the Cerenkov radiation emitted by a particle passing through a medium with a velocity  $v > c/n$  where  $n$  is the index of refraction of the medium. For a particle of momentum  $p$  and mass  $m$ , this threshold occurs at

$$n - 1 \approx m^2 c^2 / 4p^2 \quad (1)$$

For high  $p$ , the refractive index is very close to one (vacuum) and this limits the medium to a low-pressure gas. The result is a small photon flux which requires the radiator to be typically a few meters in length. For a momentum range of  $5 < p < 100$  GeV/c (the range at which CRISIS, as will be seen, can separate  $\pi$ , K, and p), one needs at least four Cerenkov pairs (each pair separating  $\pi$ , K and p and four such pairs to cover this full range). In addition, to handle high multiplicity events, each counter has to be subdivided into many cells with the consequent difficulties of separating the light emitted at finite angles by different particles. Such disadvantages in using the more conventional methods of particle identification have recently shifted attention to the possible use of ionization measurements.

## B) Identification by Ionization Sampling

An alternative method of identifying secondaries is to measure the energy loss  $dE/dx$  of a charged particle as it passes through an absorber. In low density media this energy loss rises with  $\beta\gamma$  and a measurement of it may be used to determine the velocity and, hence, the mass of the particle (Fig.2)<sup>7</sup>. The general form of the ionization for  $\beta \gg 1/137$  is given by<sup>8</sup>

$$\frac{dE}{dx} = \frac{D\rho Z}{A} \frac{1}{\beta^2} \left( \ln \frac{(\beta^2 \gamma^2)}{I} - \beta^2 + C \right) + F \quad (2)$$

where  $D=4\pi N_A r_e^2 m_e c^2 = 0.31 \text{ MeV cm}^2/\text{g}$ ,  $Z$ ,  $A$  and  $\rho$  are the charge, mass number and mass density of the medium,  $I$  characterizes the binding energy of the electrons of the medium and  $C=\ln(2m_e c^2)$ .  $F$  is a phenomenological constant negligibly small. The dependence of the ionization on  $\beta\gamma=p/mc$  has the following features:

- 1) a  $1/\beta^2$  behavior for  $\beta\gamma \lesssim 5$ ;
- 2) a minimum which depends on the type and state of the media, typically  $\beta\gamma \approx 3-10$ ;
- 3) a logarithmic rise with an eventual plateau at  $\beta\gamma \approx 300$ .

The idea was to take advantage of the logarithmic rise which, in terms of the momentum  $p$  of the ionizing particle, was predicted to extend from 5-100 GeV/c.<sup>9</sup>

#### IV THE CRISIS DETECTOR

##### A) Characteristics

CRISIS was patterned after a similar detector called ISIS (Identification of Secondaries by Ionization Sampling) developed for the CERN European Hybrid Spectrometer (EHS) by Allison et al at Oxford.<sup>10</sup> The size of our detector being a "considerably reduced" version of the Oxford ISIS, we named ours CRISIS. Since the ionization probability distribution is broad and extends to very high ionizations (Landau distribution, Fig. 3), it was necessary that multiple ionization samples be taken for each track. The result was a detector with a 1X1-m acceptance and 3 m long in the direction of the beam (Fig. 4).<sup>11</sup> Two sense planes (effectively ground), each containing 192 wires, perpendicular to the beam direction, were positioned between three high-voltage planes separated by 25.4 cm and held at a potential of -22.5 kV. A uniform electric field was achieved by two columns of field shaping tubes at the sides of the chamber. The separation of adjacent sense wires (1.6 cm) is important for the following reason. In order to minimize the ionization fluctuations in each sample and keep the channels in the detector down to a reasonable number, one would like each ionization sample to correspond to a long segment of the track. However, the collisions responsible for the ionization are not only "soft" excitations of the bound and unbound atomic states, but also involve "hard" scatters between the charged particle and the atomic electrons. Since

ener transfer is inversely proportional to the mass of the target particle, nuclear collisions can be ignored as exceptional processes in absorbers whose thickness is  $10^{-3}$  or less of an interaction length. The spectrum of energy transfer thus ranges from a few eV to the kinematic limit  $E_{\max} \approx 2m\beta^2\gamma^2c^2$  for a collision of a heavy charged particle with a free electron of mass  $m$ . The result was that 1.6 cm of 80% Argon and 20%  $\text{CO}_2$  gas at 1 atm was chosen to provide a single ionization sample. Each sample would thus contain a relatively large number of soft collisions, while keeping the probability of having a strong scatter sufficiently low to be able to disregard these samples at a later stage.

In addition to the charges, the time of arrival and the width in time of each pulse are stored. The former is necessary to reconstruct individual tracks and hybridize them with the rest of the spectrometer. The width is the time required to accumulate the charge, typically 300 nanoseconds which is approximately 1 cm in real space. The following are some useful quantitative features of the detector in terms of the digitized CRISIS time units (ctu) and charge units (ccu):

$$1 \text{ ctu} = 50 \text{ ns} = 2 \text{ mm}$$

$$\text{average pulse width} = 300 \text{ ns} = 1 \text{ cm} = 5 \text{ ctu}$$

$$\text{maximum drift time} = 6000 \text{ ns} = 25.4 \text{ cm} = 125 \text{ ctu}$$

$$\text{typical charge/ionization sample} = 0.2 \text{ pC} = 125 \text{ ccu}$$

Each CRISIS sense wire (cell) had 24 capacitors giving it the capability to store 24 charges per bubble chamber expansion (384 cells x 24 capacitors = 9216 channels total).

#### B) Reconstruction of CRISIS Planes

Since the tracks are defined by the time of arrival of the individual entries and are, therefore, one dimensional, they will be referred to as "planes". Figure 5 shows a plot of the time of arrival vs. cell number for one ping (bubble chamber expansion). A detailed description of the plane reconstruction may be found in the references.<sup>12</sup> The basic idea is the following: The first step is to take three collinear hits in three adjacent cells, make a least squares fit to the slope and intercept and then search for additional hits in subsequent cells. Any hit found to be within two least counts of the expected time of arrival is used to make a new fit. Whenever a search for the next hit in an adjacent cell fails, three possibilities may have occurred.

- 1) The plane stops at this channel because of an interaction, decay or the particle entering or leaving the chamber through the sides or high voltage planes.
- 2) The plane may have no data in the cell because of an inefficient channel.
- 3) The particle passes through the sense plane and its slope is reflected.

The possibility of channel inefficiency is dealt with by searching further along the projected plane. If the next

three cells have no data the plane is defined to have stopped. For the possibility of the track crossing the sense plane, a mirror image of the plane coordinates is made and if hits are found, the construction of the plane continues. Hits already used in the reconstruction of previous planes are not used when forming new triplets. This prevents finding the same plane over again and reduces the number of permutations for later planes. However, hits used previously may be assigned to another plane if they happen to lie within two least counts of its projection. Such hits are not used when evaluating the average ionization of a track.

### C) Survey

Two parameters must be determined before the CRISIS data can be converted into to coordinate system of real space. These are the drift velocity and T-zero. The latter is defined to be the difference between the time the beam gate is opened and the earliest time that a pulse, associated with an event from that beam, can be registered by the CRISIS electronics. These two parameters allow the time of arrival to be converted into the distance from the sense plane by the following formula.

$$D = (TOA - T_{BEAM} - T_0) \times \text{Drift Velocity} \quad (3)$$

where TBEAM is the time that the CRISIS electronics is enabled by the beam, TOA is the time of arrival of a pulse and D is the distance from the sense plane where the ionizing particle initiated the pulse.

The methods for determining these parameters are similar and rather simple. For the case of the drift velocity, planes are reconstructed in the usual manner and those that pass through the central high voltage plane are used to calculate the crossover point and, hence, the drift velocity, since the distance between the high voltage and sense plane is known to be 25.4 cm. A typical maximum drift time,  $T_{\max}$ , is about 125 least counts or 6 microseconds with an rms of 0.5 least counts (25 ns). This small variation in  $T_{\max}$ , due to the fluctuations of temperature and/or pressure, results in an error of less than 1 mm. It was found necessary to calculate the drift velocity in this manner for every roll (3000 bubble chamber pictures).

T-zero results from the electronics of CRISIS and the beam scintillators having a slightly different timing. Since this remains fixed throughout the run, it was sufficient to determine  $T_0$  once. This was done just like for the case of the drift velocity except that tracks crossing the sense plane were used to determine the cross-over point. The result was a  $T_0$  of 60 nanoseconds or about one least count.

#### D) Charge Calibration

A pulse generator was designed to calibrate each of the 9216 capacitors in CRISIS. Calibration using non-interacting beams was not sufficient for two reasons. The first is that the beam information is concentrated only on the first few capacitors in each cell. The second advantage of the pulse

generator over the beams is that the latter, although sufficient in principle to determine the pedestals for the capacitors, does not contain enough spread in the average ionizations to properly determine the gain. For example, at 200 GeV the protons and pions have an average ionization of about 120 and 127 respectively. This is not sufficient to determine the gain which will be needed for the entire Landau distribution range of 1-255.

The pulse generator sent 24 charges into each of the 384 preamplifiers at intervals which varied from 3 to 16 per microseconds. Using five different values for the input charge resulted in five simultaneous equations (for every capacitor) of the form

$$Q_{\text{out}} = P + GQ_{\text{in}} + SQ_{\text{in}}^2 \quad (4)$$

where  $Q_{\text{out}}$  was the charge measured by the electronics,  $Q_{\text{in}}$  the input charge from the pulse generator and  $P$ ,  $G$  and  $S$  were the pedestal, gain and non-linear terms respectively. The decision for a non-linear term was a result of a considerably better least squares fit its inclusion gave for most capacitors. Figure 6 shows the distributions of the three corrections and the average relation between  $Q_{\text{in}}$  and  $Q_{\text{out}}$ .

Further charge calibrations required the use of non-interacting beams. These were easily distinguished from the rest of the secondaries by making cuts on the slope, intercept and requiring at least 180 unique hits (Fig. 7). Before using these beams for calibration, three further cuts were made

(these cuts were also done on all the secondaries used later for particle identification).

- 1) Hits belonging to more than one plane (not unique) were disregarded.
- 2) Raw charges with a value of 10 or less were not used. The reason is that the electronics were protected against large charges (several pC) at the preamplifier. Whenever this occurred, the channel was grounded for 5-10 microseconds. If another charge happens to arrive at the cell during this period, it will be registered as having a value of 6 or 7.
- 3) Thirty percent of the largest remaining charges in every track are not used. There are two reasons for this. CRISIS does not have the capability to store the full range of the Landau distribution, in particular its long tail. Instead, any charge greater than 255 is stored in the overflow bin with a value of 255. The 30% cut is more than enough to exclude hits in this bin irrespective of the average ionization of the track. The second reason is that many entries in the Landau tail are a result of hard scatters with electrons (see section IV A) and including these in our ionization will introduce a large fluctuation.

An important effect which had to be corrected for was the overall gain which is the result of fluctuations in temperature, pressure and power supply voltages. It was found necessary to make such a calibration (off-line) about every 100

frames or approximately 10 minutes of data taking time. To be consistent, 100 pion, 40 kaon and 60 proton beams were selected (this was the typical beam composition during the run) and the average ionization  $\bar{I}$  determined. The overall gain coefficient was defined as  $125/\bar{I}$  and all ionizations in that interval were subsequently corrected by it. Figure 8 shows the gain corrections for several rolls.

Another calibration which made use of the non-interacting beams was the cell-to-cell variations. While the pulse generator was very useful in calibrating the electronics, it was not able to correct for any differences in the tension, thickness or potential of the sense wires which could all affect the gain in that cell. The average ionization  $I_i$  of every cell  $i$  was obtained, the total average

$$I_T = \sum_{i=1}^{384} I_i / 384 \quad (5)$$

calculated and the set of coefficients  $C_i = I_T / I_i$  were subsequently used for the correction. A  $C_i$  less than 0.6 or greater than 1.5 was set equal to zero and the cell disregarded. This cut affected only 6 out of the 384 cells. Figure 9 shows the average charges in the cells before this correction was applied.

It was discovered that an ionization sample from a beam had, on the average, a slightly larger charge when there was another pulse just preceding it. The effect is not well understood and could be due to either a "space charge" left behind by the first track or some feature of the electronics.

Figure 10 shows that this phenomena becomes important only for time differences less than 1.5 microseconds. If this is a result of a "local space charge", then it would not apply to the secondaries which are spread out in space, but only to beams which pass through CRISIS at nearly the same place (with about a 1 cm spread). An argument could be made for the electronics as being the principal cause of this effect. A pulse of ionized electrons approaching the anode sense wire will accelerate, ionize the gas further ( $\sim 0.2$  pC) and get absorbed. In the process, it will leave behind an equal charge of heavy ionized ions which will travel much slower ( $\sim m_e/A m_p$ ) toward the adjacent cathode wires. These ions could affect a second pulse of electrons in two ways: they could either absorb some of them before they reached the sense wire or screen the anode wire so that there would be a smaller amplification of the primary electrons. In both cases, the result would be a smaller average charge for the second beam, contrary to what is observed. However, it was decided not to apply the rate correction until further analysis with secondaries were performed at higher statistics.

Figure 11 is a flow chart of all the corrections made on the CRISIS raw charges leading to a final particle identification. Figure 12 shows the separation of pions, kaons and protons at the beam momentum of 200 GeV/c. The result was a width of 8.7% (FWHM/mean) and a resolution, defined as

$$R = (\bar{I}_p - \bar{I}_\pi) / \frac{1}{2} (\Gamma_p + \Gamma_\pi) \quad (6)$$

of  $R=0.60\pm 0.02$  (at 200 GeV/c momentum). Here  $\bar{I}$  is the average ionization and  $\Gamma$  is the full width at half maximum.

V THE E565/570 SOFTWARE ROUTINES

The off-line reconstruction of a bubble chamber event is a long and complicated procedure. Programs like PRECIS, GEOHYB and SQUAW have been used in high energy physics for many years. The task of every group is to modify these routines to be compatible with their data. In addition, survey parameters and titles containing unique features of the detectors have to be supplied. A detailed description of the E565/570 survey and software programs may be found in the literature<sup>13-14</sup>. Figure 13 shows the basic software logic. The data consist of two parts: a magnetic tape containing all the electronics information of the spectrometer and four rolls of film (three regular views and one high resolution) with the bubble chamber exposures. The original Fermi Lab Multi tape is "cleaned up" and the final electronics information is given a PFT format. The TRIFID program then reads this data and decides which frames should be measured by the scanners, who project the film on a table and, for every view, measure the positions of the primary and secondary vertices, points on every track (usually three) and any special feature which might be of physics interest. This information is stored on tape which, after going through several steps of format changes, is used by PEPR (Precision Encoding and Pattern Recognition)<sup>15</sup> to make accurate measurement of the bubble chamber tracks, including ionization which is done by counting the bubble density. All three views are then combined and the PRECIS

routine merges the electronics and bubble chamber measurements, evaluates the vertex positions and makes all the necessary CRISIS calibrations. CRISP provides all the coefficients for the charge corrections in CRISIS by using the PFT tape to reconstruct and identify the non-interacting beams (see section IV D). GEOHYB uses the PRECIS output to finally reconstruct an event in real space and assign each track a three-momentum. Slow tracks which don't reach the downstream spectrometer are assigned a momentum through their curvature and ionization in the bubble chamber alone, while faster particles (~50%) get hybridized with the downstream wire chambers. The final momentum resolution  $\Delta p/p$  is shown in Figure 14. The study of the electromagnetic showers in the Forward Gamma Detector is done by GAMIN which evaluates their positions and energies<sup>4</sup>. Finally, the KSQUAW-SQUAW-ARROW package makes kinematic fits to the lower topology events and is useful for identifying elastics and distinguishing  $K_S^0$ ,  $\Lambda$ , and  $\gamma$  decays in the bubble chamber.

An unexpected feature of CRISIS was that, besides being useful as a particle identifier, its well-defined planes were able to reduce the number of possible PWC and drift chamber hits to be considered for hybridization by GEOHYB. This lowered considerably the number of permutations and, therefore, the computer time for track reconstruction. There is, however, at present a problem in reconstructing CRISIS tracks and successfully hybridizing them with the rest of the spectrometer. Only 45% of all the particles entering CRISIS are hooked up and have

a useful ionization assigned to them (greater than 50 samples). Work at present indicates that this efficiency will be considerably improved in the near future.

## VI THEORY

### A) The Quark-Parton Interpretation

In the late 1960's a group at the Stanford Linear Accelerator Center (CLAC) using high energy electron beams found that the electrons scattered off proton targets with a larger transfer of momentum than had been anticipated<sup>16</sup>. This observation, analogous to the Rutherford  $\alpha$  scattering off heavy nuclei, suggested that the proton contained discrete scattering centers within. Further Deep Inelastic Scattering (DIS) experiments revealed the following observations<sup>17</sup>:

1) The valence  $u_v$  quark distribution  $xu_v(x)$  is peaked at  $x \approx 0.2$  and vanishes near  $x=1$  significantly slower than that of the valence  $d_v$  quark distribution  $xd_v(x)$ . (Here  $x$  is the Feynman scaling variable defined as  $x_F = p_{\parallel}^{\text{cm}}/p_{\text{max}}^{\text{cm}}$ .) Normalization of  $u_v(x)$  and  $d_v(x)$  is consistent with the (uud) quark picture of the proton.

2) Integrating each distribution and summing over all valence quarks shows that the total fraction of the momentum carried by valence quarks is about 50%.

3) The sea (anti)quark distribution  $xq_s(x)$  is strongly peaked at very low  $x$  values suggesting a  $1/x$  singularity in  $q_s(x)$ . Above  $x \approx 0.3$ , sea contributions are negligible. In addition, strange sea quarks are suppressed as compared to non-strange ones by a factor of about 0.3. The integral over the sea quark distributions yields only about 5% as an average fraction of the total proton momentum, thus leaving about half of the momentum unaccounted for. This is presumably carried

by gluons which, as predicted by QCD, are flavor-neutral and, therefore, "invisible" to the electromagnetically and weakly interacting leptons. These and other results showed that valence quarks, while very useful in categorizing the overwhelming number of hadron states, are not sufficient to describe the experimentally observed properties of multiparticle yields. The constituents of hadrons, therefore, are commonly referred to as "partons" and include valence and sea quarks as well as the gluons.

#### B) Models

The development of parton ideas, the identification of partons with quarks and gluons and the introduction of QCD perturbative calculations were all related to high momentum transfer or "hard" processes. The properties of low momentum transfer or "soft" processes, although responsible for the bulk of hadron production in high energy collisions, have, until recently, received little attention. With the formulation by Feynman<sup>18</sup> of a general parton picture of inclusive and exclusive hadron-hadron processes, a new interest in quark models has emerged in the last few years. The first application to soft processes has been presented by Goldberg<sup>19</sup>, who interpreted the relatively fast decrease of the Feynman  $x$  spectra of mesons in the proton fragmentation region as a reflection of the valence quark structure function in the initial proton. This idea, rediscovered by Ochs in 1977<sup>20</sup>, has become the origin of various so-called recombination models<sup>21</sup>.

## C) The Quark Recombination Model

The basis of the Quark Recombination Model (QRM) stems from the observation that fast secondary mesons containing one of the valence quarks of the hadron beam have a longitudinal momentum spectrum largely determined by the momentum carried by these quarks before the collision. This explains the success of the phenomenological relation

$$\frac{1}{\sigma} \frac{d\sigma}{dx}(a \rightarrow M) F_q^a(x) \quad (7)$$

where  $q$  is the valence quark common to the hadron  $a$  and meson  $M$  and the DIS structure function  $F_q^a(x)$  describes the  $x$  distribution of the valence quark  $q$  in the hadron  $a$ . A similar relation holds for baryon production having a common diquark with the initial hadron, although the diquark  $x$  distribution is more difficult to evaluate from DIS. The first detailed recombination model was proposed by Das and Hwa<sup>22</sup> who assumed that relation (7) is only an approximation. Their equations take into account the recombination of the valence quark  $q_v$  and sea antiquark  $q_s$  into the final meson  $M$

$$\frac{1}{\sigma} \frac{d\sigma}{dx}(a \rightarrow M) = C \int \int F_{q_v}^a(x_1) F_{q_s}^a(x_2) (1-x_1-x_2) R(x_1, x_2, x) (x-x_1-x_2) dx_1 dx_2 \quad (8)$$

where there are now two structure functions multiplied by a phase space factor  $(1-x_1-x_2)$ .  $R$  is the recombination function.



There are several difficulties with this model, especially in the low  $x_F$  region. The violation of exact scaling (the constituents of a hadron depend on the momentum transfer  $Q^2$  of the leptons in DIS, e.g., the number of visible constituents in a proton increases with resolution) means that the structure functions, as measured in deep inelastic lepton-hadron scattering, are not unique, but depend on  $Q^2$ . Although for a moderate  $Q^2$  in the range of 1-5 GeV<sup>2</sup> and for reasonably large  $x$  ( $x > 0.2$ , say)<sup>21</sup> scaling effects are not very crucial; they become important in the central region where the number of sea quarks grows as  $1/x$ . Another problem with QRM is that caution must be taken when one tries to apply the model to the production of particles which have no valence quarks in common with the initial hadrons. These should be formed from the sea quarks and antiquarks alone (called "unfavored" processes). While the general predictions at high  $x$  are confirmed experimentally in many cases, the quantitative description is less successful. Finally, the recombination function  $R$  in equation 8 is rather arbitrary at best. The original choice for  $R$

$$R(x_1, x_2, x) = C x_1 x_2 / x^2 \quad (9)$$

where  $C$  could be a smooth function of  $x_1/x_2$ , and a later one suggested by Takasugi et al.<sup>23</sup>

$$R(x_1, x_2, x) \propto e^{-D(y_1 - y_2)^2} \quad (10)$$

where the adjustable parameter  $D \approx 0.5$ , give similar results. Efforts are still under way in reducing the arbitrariness of  $R$ . Results from photoproduction experiments and  $J/\psi$  decay support the original choices for  $R$ .

#### D) Quark Fragmentation Models

For a long time there have been indications that jets are "universal" in the sense that the main features of hadron production along some specific momentum axis, usually the beam, are the same in all types of collisions. A quantitative version of this idea has been proposed by Andersson et al.<sup>24</sup> who observed the similarity between the Feynman  $x$  distribution in meson meson fragmentation processes and the quark meson fragmentation functions, as determined in  $e^+e^-$  and lepton-hadron experiments. The model, referred to as the "quark fragmentation model" (QFM) assumes that a hadron-induced fragmentation can be described in two steps. In the first step, two valence quarks, one from each hadron, carrying a rather small fraction of the total momentum interact. In the second step, the "remaining hadron", carrying most of the momentum and quantum numbers of the original hadron, fragments into the final state mesons and baryons by the same mechanism as the quark(s) in  $e^+e^-$  jets and lepton-hadron collisions. In general, a meson  $M$  or baryon  $B$  fragmenting into hadron  $h$  can be expressed, respectively, as

$$\frac{1}{\sigma} \frac{d\sigma}{dx}(M \rightarrow h) = 1/2 (D_h^{q1}(x-\Delta x) + D_h^{q2}(x-\Delta x)) \quad (11)$$

$$\frac{1}{\sigma} \frac{d\sigma}{dx}(B \rightarrow h) = (1/3) \sum_{i=1}^3 D_h^{(qq)i}(x-\Delta x) \quad (12)$$

where  $\Delta x$  denotes the average fraction of the initial momentum lost with the interacting quark,  $(qq)_i$  represents the valence diquark left after removing quark  $q_i$  from the baryon and  $D_h^q(x)$  are the fragmentation functions of  $q_1$ ,  $q_2$  or  $qq_i$  into hadron  $h$ .

One drawback of equations (11) and (12) is that they ignore the structure functions of the initial hadrons. In particular, there is no attempt to evaluate  $\Delta x$ , the momentum lost in the collision, which depends on the type of hadron fragmenting. As a consequence, a "dual QFM" was developed. It was originally motivated by the connection between the string and dual resonance models and later formulated into the dual topological unitarization scheme (DTU)<sup>25</sup>. One of its outcomes was that equations (11) and (12) are only approximations to the correct relations

$$\frac{1}{\sigma} \frac{d\sigma}{dx}(M \rightarrow h) = \frac{1}{2} \int_x^1 (F_{q_1}^M(1-x') D_h^{q_2}(x/x') + F_{q_2}^M(1-x') D_h^{q_1}(x/x')) dx' \quad (13)$$

$$\frac{1}{\sigma} \frac{d\sigma}{dx}(B \rightarrow h) = (1/3) \sum_{i=1}^3 \int_x^1 (F_{q_i}^B(1-x') D_h^{(qq)_i}(x/x')) dx' \quad (14)$$

The shape of the structure functions  $F_q^h(x)$  can be predicted from the model for the limits  $x \rightarrow 0$  and  $x \rightarrow 1$  and are not necessarily identical to those of valence quarks as seen in DIS.

The present data will be compared to one of the first versions of the QFM which is based on a semiclassical string concept. In such a picture, an initial color exchange between a pair of relatively slow partons produces two strings with the

ends being "slow" and "fast" triplet color charges. The model further assumes that the fragmentation functions are the same as those in analogous strings in  $e^+e^-$  and lepton-hadron interactions, provided the flavor quantum numbers of the fast string ends are chosen correspondingly. This version of the QFM has become known as the "Lund Model" whose recent success has made it the most commonly used tool to investigate acceptances and experimental biases in high energy physics. Since it is based on results from quark jets (especially from  $e^+e^-$  colliders) and makes a limited use of the hadron structure functions, one would not expect it to be very precise in predicting accurately hadron-hadron data in the extreme fragmentation regions. However, since in the central region the effects of the original hadron flavors are presumably negligible, there is reason to expect the model to work as well there as it does in explaining  $e^+e^-$  and lepton-hadron interactions.

#### E) The Lund Model

In this model a hadron is pictured as an extended object, or bag, containing color which is confined by the surrounding vacuum pressure<sup>27-29</sup>. When two such objects collide, there will be an overlap between the bags which may remain connected when the hadrons begin to separate (Fig. 15a). In particular, it is assumed that two constituents, or partons, one from each bag, interact and join while the remaining are essentially unaffected. Initially, the constituents are just the valence quarks which, in the framework of a semiclassical string model,

are joined by a linear color force field. Results from charmonium spectroscopy and bag model calculations indicate that a string constant of  $1 \text{ GeV/fm} \approx 0.2 \text{ GeV}^2$  is a reasonable approximation.

The non-interacting valence quarks will continue to move along their original direction until all of the energy is used up to produce the force field behind them. When this happens, there will be an essentially one-dimensional color field with one of the valence flavors at each end. However, long before the total energy gets transferred into the field, the color string will break and produce a new  $q\bar{q}$  pair. Several breaks may take place in this manner after which a recombination process will produce resonances and stable hadrons. For example, a  $\bar{q}_1$  from a  $q_1\bar{q}_1$  pair may join a  $q_2$  from a  $q_2\bar{q}_2$  pair to form a  $\bar{q}_1q_2$  color singlet meson.

Besides assuming a universal linear field between the two quarks (equal for all flavors), the second hypothesis made by the Lund Model is that, given a stretched string of length  $L_0$ , a pair of massless  $q\bar{q}$  particles with zero momentum can be produced at any point inside the field with constant probability per unit length

$$\frac{dP}{dL} = \text{constant} = 1/L_0 \quad (15)$$

In the frame where one of the ends of the string is at rest ( $q_0$  in Fig. 15b, say), a variable  $z_1$  is defined as the fraction of the available momentum  $p_0$  that a newly formed meson  $q_0q_1$  in the cascade can take away from the color field

$$z_1 = p / p_0 = (L_0 - L_1)L/0 \quad (16)$$

where  $L_1$  is the distance from the  $q_1\bar{q}_1$  production to the end of the string which is at rest ( $q_0$  quark). In terms of  $z_1$ , equation 15 can be written as

$$\frac{dP}{dz_1} = 1 \quad (17)$$

It should be pointed out that the original and best known jet generation scheme, the Field-Feynman Model (FF),<sup>30</sup> is similar in many respects. The major difference is in the longitudinal fragmentation. There, instead of a constant  $dP/dz$ , the relation  $dP/dz=1-a+3az^2$  is used where the parameter  $a=0.77$  is obtained from fits to experimental data.

A similar way of defining the scaling variable  $z$  is

$$z = \frac{p}{p_0} \approx \frac{(E+p_{||})}{2p_0} \quad (18)$$

This allows the fragmentation scheme to become Lorentz invariant under boosts along the beam direction. The "rapidity", defined by

$$y_z = -\ln(z) = -\ln\left(\frac{E+p_{||}}{2p_0}\right) \quad (19)$$

and related to the usual rapidity  $y=1/2\ln((E+p_{||})/(E-p_{||}))$  by

$$y = -y_z = -\ln(2p_0/m_T) \quad (20)$$

is a convenient variable for fragmentation studies because it does not depend on the generated value of the perpendicular mass  $m_T = (m^2 + p_T^2)^{1/2}$ . In terms of  $y_z$ , equation (17) then takes on a simple form

$$\frac{dP}{dy_z} = -e^{-Y_z} \quad (21)$$

This distribution, as will be seen, agrees well with our data.

For the next break,  $q_2 \bar{q}_2$ , in the cascade process, a Lorentz boost is made so that now  $q_1$  is at rest. When the newly formed meson  $q_0 \bar{q}_1$  is taken away, the rest looks just like the original jet when expressed in terms of the new scaling variable  $z' = z/(1-z_1)$  where  $(1-z_1)$  is the factor by which the total energy has been reduced.

The model requires that each  $q\bar{q}$  pair be flavorless. This means that if the original quark had flavor  $a$  and the pair  $q\bar{q}$  have flavor  $b\bar{b}$ , then the meson  $q_0 \bar{q}_1$  must have flavor  $a\bar{b}$  whereas meson  $q_1 \bar{q}_2$  has flavor  $b$  etc. This produced a recursive integral equation

$$D_a^{bc}(z) = \delta_{ab} f_c + \sum_d \int \frac{dz'}{z-z'} f_d D_d^{bc}(z/z') \quad (22)$$

where  $D_a^{bc}(z)$  is the fragmentation function for a quark with flavor  $a$  producing a meson  $b\bar{c}$ , and  $f_c$  is the relative probability to produce a  $q\bar{q}$  pair with flavor  $c\bar{c}$  ( $\sum_c f_c = 1$ ).

The model predicts that the mesons will be ordered according to flavor "rank" because the produced  $q\bar{q}$  pairs have a total flavor of zero. However, due to the stochastic nature

of the production process, flavor ordering will reflect itself in rapidity only on the average. In addition, ordering according to production time is Lorentz frame dependent. In this scheme, the slowest particles will be the first to get separated from the jet in each frame.

Without going into further details, a list of some of the more important features and parameters of the Lund Model are given.

- a) For heavy mass  $q\bar{q}$  pairs, a production rate factor  $e^{-(\pi m_T^2/k)}$  must be included for each vertex. This suppresses the production of the heavier quarks ( $u:d:s:c^{\sim}1:1:0.3:10^{-11}$ ).
- b) The probability  $dP/dz$  is modified a little due to the softening of the  $z$  spectrum from gluon effects.
- c) Baryons are formed in a way analogous to that of the mesons by using diquark-quark combinations. Suppression of  $qq, \bar{q}\bar{q}$  pair production relative to  $q, \bar{q}$  is equal to  $P(qq)/P(q)=0.075$ .
- d) Strange particle suppression:  $P(s)/P(d)=0.3$  for quarks and  $(P(us)/P(ud))/(P(s)/P(d))=0.2$  for diquarks.
- e) Relative production of pseudoscalar and vector mesons is assumed equal (a 1:3 ratio predicted from SU(6) spin counting is not supported by experiments which seem to indicate a 1:1 ratio).
- f) Diagonal flavor combinations  $u\bar{u}$ ,  $d\bar{d}$  and  $s\bar{s}$  are mixed to produce pseudoscalar and vector mesons ( $\pi^0$ ,  $f^0$  etc.).
- g)  $P(S=3/2 \text{ baryons})/P(S=1/2 \text{ baryons})=2$  from spin counting.
- h) Primary hadrons have a gaussian  $p_T$  distribution with a width  $\sigma = .44 \text{ GeV}$ .

i) All particles have masses, widths and branching ratios according to the particle data tables.

j) Resonances with spin  $\geq 2$  are not incorporated.

## VII THE CRISIS PARTICLE IDENTIFICATION ALGORITHM

After hybridizing the secondaries, evaluating their momentum and applying all the necessary calibration corrections to the CRISIS raw charges (section IV-D), it was necessary to obtain an ionization curve similar to that of Fig. 2. The easiest way to see the separation between the pions, kaons and protons was to select a small momentum interval and plot the average ionization distribution of all the secondaries containing CRISIS charge information (Fig. 16). A 2.5 GeV/c momentum bin was found to be the best choice for two reasons: a smaller value was not possible because of low statistics while a larger range would considerably reduce the resolution, especially at low momentum where  $d(dE/dx)/dp$  is large. The solid curves in Fig. 16 represent a fit to the data using three gaussian distributions with centers, heights and widths being variable parameters. Figure 17 shows the ionization curves for the  $\pi$ 's, K's and p's, obtained by fitting

$$\bar{I} = A/\beta^2 (\ln(p) - \beta^2 + B) \quad (23)$$

to the gaussian centers in Fig. 16. Here  $\bar{I}$  is the average ionization in CRISIS charge units,  $\beta = v/c = p/mc\gamma$  and A and B are two free parameters. One might, in principle, obtain the ionization curves for the kaons and protons from the pion curve alone, which is known to a better accuracy. Since the ionization is a function of  $\beta\gamma$  only (assuming a fixed medium and neglecting effects due to the spin of the ionizing particle), the point  $(p, I)$  on the pion curve, for example, would correspond

to the point  $(p_{\pi}/m_K, I)$  on the kaon curve. The problem with this approach is that the portion of the pion ionization curve that is to be used for such a transformation corresponds to a momentum less than 10 GeV/c. In this region the statistics are very low (secondaries with momentum less than 5-6 GeV/c never reach CRISIS) and the position of the pion curve is not very precise. Since  $dI/dp$  is very large there, one would not expect this technique to provide an accurate calculation of the kaon and proton ionization curves.

For a fixed momentum, the width  $\sigma$  of the three gaussian distributions was assumed to be equal (data from tagged beams supports this). Therefore, using the pion ionization width  $\sigma$  as the standard, Fig. 18, which shows a linear fit to  $\sigma$  as a function of momentum, was obtained. The small increase of the width with decreasing momentum was assumed to be the result of taking a greater slice of the ionization curve for a fixed  $\Delta p = 2.5$  GeV/c at low  $p$  values where  $dI/dp$  becomes large. It was, therefore, decided to use a constant  $\sigma = 4.9$  throughout.

It is clear from the data that a complete separation between the three particles is not possible. Therefore, an algorithm which would assign a probability that a given CRISIS track is a pion, kaon or proton was necessary. For this purpose, Bayes Theorem was used. The idea is the following.

Assume 3 possible reactions a,b,c ( $\pi, K, p$  gaussian distributions) and a measurable stochastic outcome  $Q$  (the average ionization). Let  $(Q, r)$  be the likelihood of  $Q$  given reaction

$r \in (a, b, c)$  and let  $p_r$  be the probability of cause  $r$ . Then Bayes Theorem states that the odds of  $r$  given  $Q$  is

$$f(r, Q) \propto (Q, r) p_r$$

Letting  $s = \sum_r (Q, r) p_r$ , the probability of  $r$  given  $Q$  is then

$$f(r, Q) = \frac{(Q, r) p_r}{s} \quad r \in (a, b, c) \quad (24)$$

For the present case, the gaussian curves  $e^{-(Q-\bar{Q})^2/2\sigma^2}$  for the three particle types correspond to the likelihoods  $(Q, r)$  in Bayes Theorem while the relative heights of these curves give the probability  $p_r$  for each of the distributions. It should be noted that the plots in Fig. 16 include all three beams and both, positive and negative secondaries. Although this is sufficient to determine the ionization centers and widths, it fails to give the correct particle yields which depend on beams and the sign of the secondaries (in addition to the energy and angles). Since our statistics were too low for further separating each histogram in Fig. 16 into six categories, inclusive single particle productions were determined by the Lund Model Monte Carlo 43G routine<sup>29</sup>.

The software package for the Lund Monte Carlo requires only the initial condition of an interaction. Fragmentations, recombinations and decays are simulated according to the ideas discussed in section (VI-E). For the present case, this consisted of a proton target with a (uud) valence quark content interacting with three different positive beams ( $\pi^+(u\bar{d})$ ,  $K^+(u\bar{s})$ , and  $p(uud)$ ). The goal was to simulate an event as

closely as possible to a real one and use only those charged particles that should have gone through CRISIS to estimate the relative yields in that detector. The following conditions were required.

a) The Lund model assumes that one valence quark from the hadron beam interacts with another valence quark in the target. Equal probabilities were, therefore, assigned for all possible quark combinations. A  $K^+(u\bar{s})p(uud)$  interaction, for example, has six combinations.

b) The vertex of each interaction was given the same  $x, y, z$  bubble chamber coordinate distribution as the real data (Fig. 19).

c) After the unstable particles were allowed to decay, all charged secondaries were swum through the magnetic field and those that should have entered CRISIS were used to determine the particle distributions.

Figure 20 shows the Lund Monte Carlo predictions for the production of kaons and protons, grouped according to the beam type and the particles' charge. Note that, for a given beam, charge and momentum,  $P(\pi^+) = 1 - P(K^+) - P(p)$  and similarly  $P(\pi^-) = 1 - P(K^-) - P(\bar{p})$  where  $P(x)$  is the fraction of all the particles of type  $x$ . As a check, a similar simulation was made and compared to data from a counter experiment<sup>31</sup> which looked at single particle distributions in  $\pi^+p$ ,  $K^+p$  and  $pp$  interactions at 100 GeV/c beam momentum (Table I). The two results agree rather well.

Figure 21 shows a typical probability assignment by the CRISIS algorithm where, as an example, a positive secondary particle produced in a  $\pi^+p$  interaction and having a momentum of 15 GeV/c was chosen. The efficiency of CRISIS in identifying a kaon peaks at about 65% for a proton and pion beam and 75% for a kaon beam (Fig. 22).

### VIII RESULTS

Before using the CRISIS algorithm to identify secondaries and study specific physics topics, it was necessary to check its performance against some of the better established experimental and theoretical results. The simplest way was to compare single particle production. This, however, required a precise knowledge of the CRISIS acceptance. In particular, only those particles which enter the front face of CRISIS ( $1 \times 1 \text{ m}^2$ ) after traveling 5 meters from the bubble chamber (part of the way through a magnetic field) should be considered. It was decided to resort again to the Lund model which was seen to be in agreement with the 100 GeV data of Ref. 31 where Cerenkov counters were used to identify the secondaries (Table I). A comparison with the present data is shown in Table II. As discussed in the last section, the Lund Monte Carlo results were obtained by swimming every charged secondary through a magnetic field similar to ours and using only those particles that would have entered CRISIS. The particles in the real data were given a weight equal to the probability assigned to them by the algorithm. The agreement is rather good with the exception of a small difference in the proton and antiproton production from the  $\pi^+$  and  $K^+$  beams. The results, however, are compared to the particle yields predicted by the model which, in turn, was used in developing the algorithm in the first place.

A better way of testing the reliability of CRISIS is to look for specific resonances which should emerge if the

algorithm assigns the correct probabilities to the different particles. A strong  $K^{*0}, \bar{K}^{*0}(890)$  signal, for example, is expected in a  $K^+p$  interaction if an invariant mass  $M(K^+\pi^-)$  is used with the K in the positive rapidity region. Figure 23a shows the background obtained by assuming every charged particle in CRISIS to be a kaon and using any other oppositely charged particle as a pion to calculate  $M(K\pi)$ . Figure 23b is a result of weighing a track in CRISIS by the probability that it is a kaon. A  $K^*$  signal is seen near 880 MeV and agrees well with the Lund model (Fig. 23c). In particular, the ratios of  $K^{*0}/K^\pm = 13 \pm 4\%$  and  $K^{*0}/K^+p \text{ event} = 4.9 \pm 1.6\%$  agree well with the model's predictions of  $12 \pm 2\%$  and  $5.0 \pm 0.7\%$  respectively (the  $K^*$  and K's are those that are detected by CRISIS). To obtain the cross section, a Lund model calculation was used to give 17% as the fraction of all the  $K^{*0}(890)$ 's produced in  $K^+p$  interactions at 200 GeV/c which will decay into  $K^+\pi^-$  with the charged kaon entering CRISIS. A simulation of 4000  $K^+p$  events ( $\sigma_\tau = 20$  mb at 200 GeV) produced 1185  $K^{*0}$ 's. Correcting our  $K^{*0}$  production by the 45% CRISIS hybridization efficiency factor and using the above acceptance calculation, gave a total cross section for  $K^+p \rightarrow K^{*0} + X$  of  $\sigma_\tau = 5.3 \pm 1.6$  mb compared to the Lund model's  $\sigma_\tau = 5.9 \pm 0.2$  mb. In addition to the  $K^*(890)$  resonance, a small  $K^*(1430)$  signal is seen in our data (the Lund model, which does not consider particles of spin 2 and greater, has no corresponding signal). In a similar manner, a  $\Delta^{++}$  resonance (Fig. 24) is seen in pp events. As before, each  $M(p\pi^+)$  entry is weighed by the probability that a positive

track in CRISIS is a proton. The total cross section obtained for the reaction  $pp \rightarrow \Delta^{++} + X$  was  $\sigma_T = 5.7 \pm 1.6$  mb compared to  $6.9 \pm 0.3$  mb predicted by the Lund model. Finally, given our statistics, CRISIS acceptance and using all three beams, the model predicts that only about 4  $\phi$ 's should be produced. Figure 25a shows an invariant mass  $M(K^+K^-)$  distribution assuming every positive (negative) particle in CRISIS to be a  $K^+$  ( $K^-$ ). Figure 25b is a similar plot weighted by the probability that a given track is not a kaon. A small  $\phi(1020)$  signal, seen in Figure 25a, disappears. Figure 25c uses the weight that both  $K^+$  and  $K^-$  in  $M(K^+K^-)$  are kaons. The result agrees well with that predicted.

#### Short Range Correlations

It is widely believed that in multiparticle production the final formation of hadrons in the central region is governed by small- $Q^2$  phenomena which generate local short-range correlations (SRC). In the final stages of the fragmentation process, it is assumed that a sea quark pair  $q\bar{q}$ , once produced, will either stay together and form a color singlet meson or separate and recombine with nearby quarks to produce hadrons. In both cases, the original  $q\bar{q}$  quarks should end up very close to each other. As a result of the small number of strange quarks produced in typical high energy events, looking for strange particle correlations is a relatively clean way to study the fate of the  $q\bar{q}$  quark pair. In order to reduce the effects of valence quarks, only  $\pi^+p$  and  $pp$  events with a

topology of 4 or greater were selected. The particles were then ordered according to their rank in rapidity. The number  $n$  will represent how far apart two particles are in this ordering scheme. For example, in the situation

$$\dots K^+ \pi^- \pi^+ K^- \dots \rightarrow y$$

the two K's are separated by  $n=3$ . Figure 26a shows the separation  $n$  for all particles in CRISIS with the rapidities calculated by assuming every particle to be a pion. This is just the background defined to have zero correlation. The reason that it is peaked at  $n=1$  comes from two factors. The first is simply a result of taking all possible combinations. For example, if there are three tracks in CRISIS, there will be two entries for  $n=1$  and only one for  $n=2$ . The second reason comes from the fact that the average number of tracks in CRISIS is rather low. This background was subtracted from further  $n$ -distributions to better enhance any correlations (each bin was divided by the content of the corresponding bin of Figure 26a and a flat distribution will, by definition, represent zero correlation). Figure 26b shows a small correlation between an arbitrary positive and negative particle in CRISIS. A much stronger correlation is observed in Figure 26c. This represents the separation between two oppositely charged kaons. In Figures 27a-e, one can see the effect of making different cuts on the probability for a particle to be a kaon (10%-30%). The data was normalized such that the contents of the first bin would be 100. Figure 28 is a comparison of our data with

the Lund model. Such a correlation is not expected in a  $K^+p$  event where one of the kaons contains the original beam valence quark and the other is produced from the sea. Figure 29 shows that such an "anticorrelation" does indeed exist. Finally, Figure 30 compares the strangeness correlation in the true rapidity. Here again the idea of local flavor conservation is supported.

Short range  $K^+K^-$  correlations were recently reported at PEP using the time projection chamber (TPC)<sup>32</sup>. Flavor correlations in pp collisions<sup>33</sup> also seem to support the picture of "local strangeness".

## XI CONCLUSIONS

The possibility of identifying elementary particles by using multiple ionization sampling is supported by the CRISIS detector. It has the disadvantages of not being useful as a triggering device and unable to fully separate pions, kaons and protons. The probabilities that it can assign to these particles, however, makes it useful for studying a wide range of topics where high statistics are available. In addition, its capability of identifying several particles over a wide momentum range makes it unique.

The observed short range strangeness correlation supports the idea of local flavor conservation. Comparison with the Lund model indicates an even stronger correlation. This could be explained by several factors.

1) A statistical fluctuation is possible but not likely (Figure 28).

2) If too many resonances which decay into charged kaons had been produced by the model, a reduced strangeness correlation would have been expected. The good agreement with the  $K^*$  and  $\phi$  production does not seem to support this.

3) In a linear force field  $k$  (1 GeV/fm in the Lund model), a massive  $q\bar{q}$  pair is produced with a probability proportional to  $e^{-(\pi m_T^2/k)}$ . The smaller average  $n$  observed in our data (Figure 28) could be due to a fewer number of  $q\bar{q}$  pairs produced in a field between an  $s$  and  $\bar{s}$  quark. This might suggest a stronger field  $k$  between the strange quarks than between the  $u$  and  $d$  quarks. The agreement with the topology and rapidity

distributions (Figure 31), however, suggests that the value of  $k=1$  GeV/fm works well for the general fragmentation process. Since this value is also well supported by results from charmonium spectroscopy, the string constant, as predicted by theory, should be independent of flavor. There is no reason, therefore, why an exception should be made for the case of strangeness.

REFERENCES

1. Gell-Mann M. Phys. Lett. 8 214 (1964)
2. Zweig G. CERN Preprints CERN-TH 401 412 (1964)
3. P. Haridas and S. Noguchi, "The High Resolution IHSC Camera at the Fermilab 30" H2 Bubble Chamber", APC Engineering Note 82-7 (1982) (unpublished)
4. Bober J. MIT Ph.D. Thesis (1984)
5. Taft H. and Steiner R., "E-570 Multi Modifications" (1981) (unpublished)
6. Bethe H. and Jackie R. Intermediate Quantum Mechanics pp. 302-5, New York: Benjamin (1968)
7. Bethe H. Ann. Phys. 5 325 (1930)
8. Fano U. Ann. Rev. Nucl. Sci. 13 1 (1963)
9. Allison W. and Cobb J. Ann. Rev. Nucl. Part. Sci. 30 253 (1980)
10. Allison W. et al Nucl. Inst. Meth. 119 499 (1974)
11. Alyea E. et al Rev. Sci. Instrum. 53(4) 393 (1982)
12. Goloskie D. et al, "The Performance of CRISIS and Its Calibration", submitted to Nucl. Instrum. & Methods, August 15, 1984. The design and construction of CRISIS was supervised by Vera Kistiakowsky.
13. DeMarco R., Rutgers Ph.D. Thesis (1985)
14. Frank T., MIT Ph.D. Thesis (1985)
15. Pless I., IEEE Transactions on Nucl. Phys. 279 Aug. 1965
16. Panofsky W., Proceedings of International Symposium on High Energy Physics, Vienna (1968)
17. Close F., An Introduction to Quarks and Partons, New York: Academic (1979)

18. Feynman R., Phys. Rev. Lett. 23, 1415 (1969)
19. Goldberg H., Nucl. Phys. B44 149 (1972)
20. Ochs W., Nucl. Phys. B118 397 (1977)
21. Fialkowski K. and Kittel W., Rep. Prog. Phys. 46 1282 (1983)
22. Das K. and Hwa R., Phys. Lett. 68B 459 (1977)
23. Takasugi E. et al. Phys. Rev. D20 211 (1979)
24. Andersson B. et al. Phys. Lett. 69B 221 (1977)
25. Veneziano G., Nucl. Phys. B117 519 (1976)
26. Capella A. et al. Phys. Lett. 81B 68 (1979)
27. Andersson B. et al. Lund preprint LU TP 80-5 (1980)
28. Andersson B. et al. Z Physik C. 1 105 (1979)
29. Sjostrand T., Computer Phys. Communications 27 243 (1982)
30. Field R. and Feynman B., Nucl. Phys. B136 1 (1978)
31. Barton D. et al. Phys. Rev. D27 2580 (1983)
32. Aihara H. et al. Phys. Rev. Lett. 53 2199 (1984)
33. Breakstone A. et al. Z. Phys. C25 21 (1984)

TABLE I

Comparison between the data of Ref. 31 and the Lund model for reactions  $\pi^+p$  and  $pp$  at 100 GeV/c momentum. The numbers represent particle productions relative to all the stable charged particles ( $\pi, K, p$ ). ( $25 \leq p \leq 35$  GeV/c,  $0.24 \leq p_T \leq 0.40$  GeV/c)

<u>Particle</u>	<u><math>\pi^+</math> BEAM</u>	
	<u>LUND</u>	<u>Ref. 31</u>
$\pi^+$	$60.5 \pm 2.3\%$	$53.7 \pm 1.8\%$
$K^+$	$5.9 \pm 0.7$	$5.5 \pm 1.0$
$p$	$4.5 \pm 0.6$	$5.5 \pm 1.0$
$\pi^-$	$22.7 \pm 1.4$	$29.7 \pm 1.2$
$K^-$	$4.3 \pm 0.6$	$3.4 \pm 0.6$
$\bar{p}$	$2.0 \pm 0.4$	$2.2 \pm 0.3$

<u>Particle</u>	<u><math>p</math> BEAM</u>	
	<u>LUND</u>	<u>Ref. 31</u>
$\pi^+$	$30.5 \pm 2.1\%$	$36.5 \pm 1.8\%$
$K^+$	$5.4 \pm 0.9$	$6.4 \pm 1.1$
$p$	$36.7 \pm 2.3$	$37.3 \pm 1.9$
$\pi^-$	$23.4 \pm 1.8$	$18.0 \pm 1.1$
$K^-$	$2.8 \pm 0.6$	$1.3 \pm 0.5$
$\bar{p}$	$1.2 \pm 0.4$	$0.6 \pm 0.3$

TABLE II

Inclusive charge particle production in CRISIS  
(200 GeV/c)

<u>Particle</u>	<u><math>\pi^+</math> BEAM</u>	
	<u>DATA</u>	<u>LUND</u>
$\pi^+$	46.6 $\pm$ 2.5%	52.2 $\pm$ 1.1%
$K^+$	4.8 $\pm$ 0.8	4.7 $\pm$ 0.3
p	7.8 $\pm$ 1.0	4.4 $\pm$ 0.3
$\pi^-$	34.5 $\pm$ 2.2	32.7 $\pm$ 0.9
$K^-$	5.7 $\pm$ 0.9	4.2 $\pm$ 0.3
$\bar{p}$	0.7 $\pm$ 0.3	1.8 $\pm$ 0.2

<u>Particle</u>	<u><math>K^+</math> BEAM</u>	
	<u>DATA</u>	<u>LUND</u>
$\pi^+$	36.8 $\pm$ 2.8	42.4 $\pm$ 1.3
$K^+$	11.2 $\pm$ 1.6	13.6 $\pm$ 0.7
p	8.4 $\pm$ 1.4	4.7 $\pm$ 0.4
$\pi^-$	37.7 $\pm$ 2.9	31.8 $\pm$ 1.1
$K^-$	5.4 $\pm$ 1.1	4.2 $\pm$ 0.4
$\bar{p}$	0.5 $\pm$ 0.3	3.3 $\pm$ 0.4

TABLE II (continued)

<u>Particle</u>	<u>p BEAM</u>	
	<u>DATA</u>	<u>LUND</u>
$\pi^+$	$41.7 \pm 2.4\%$	$44.1 \pm 1.1\%$
$K^+$	$5.0 \pm 0.8$	$5.6 \pm 0.4$
p	$10.0 \pm 1.2$	$11.5 \pm 0.6$
$\pi^-$	$36.5 \pm 2.3$	$32.8 \pm 1.0$
$K^-$	$5.7 \pm 0.9$	$4.0 \pm 0.3$
$\bar{p}$	$1.7 \pm 0.5$	$2.0 \pm 0.2$

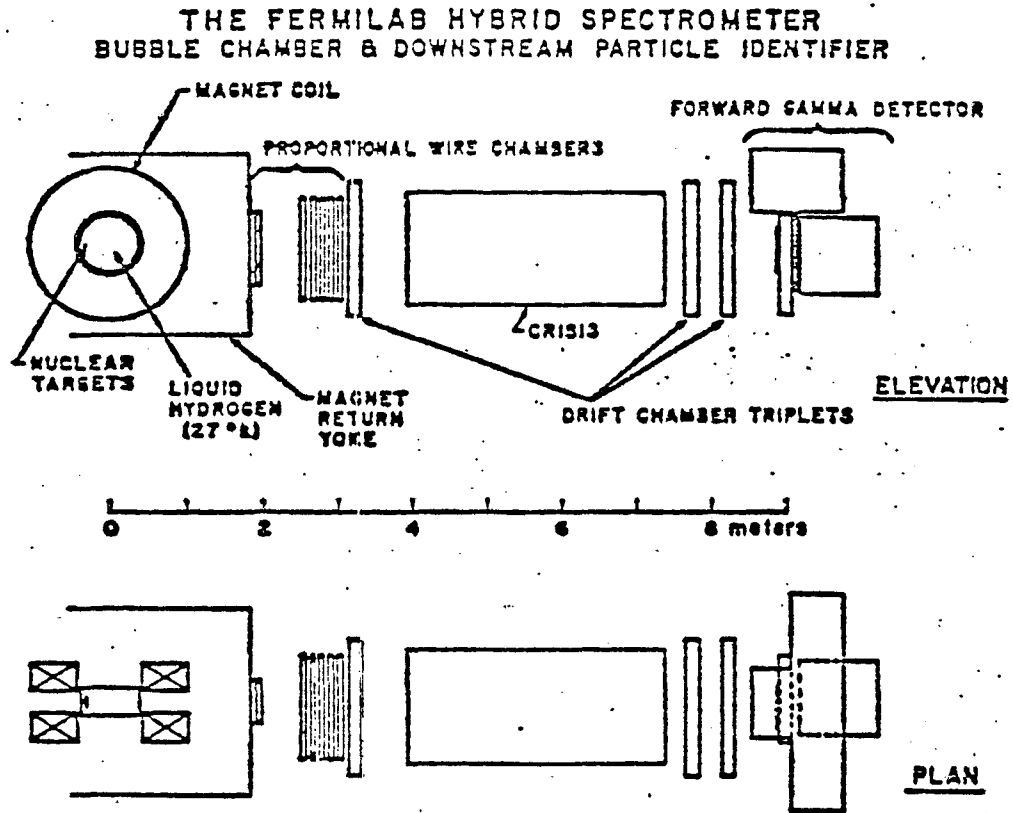


Fig. 1. Side and top view of the downstream hybrid spectrometer (Ref. 14).

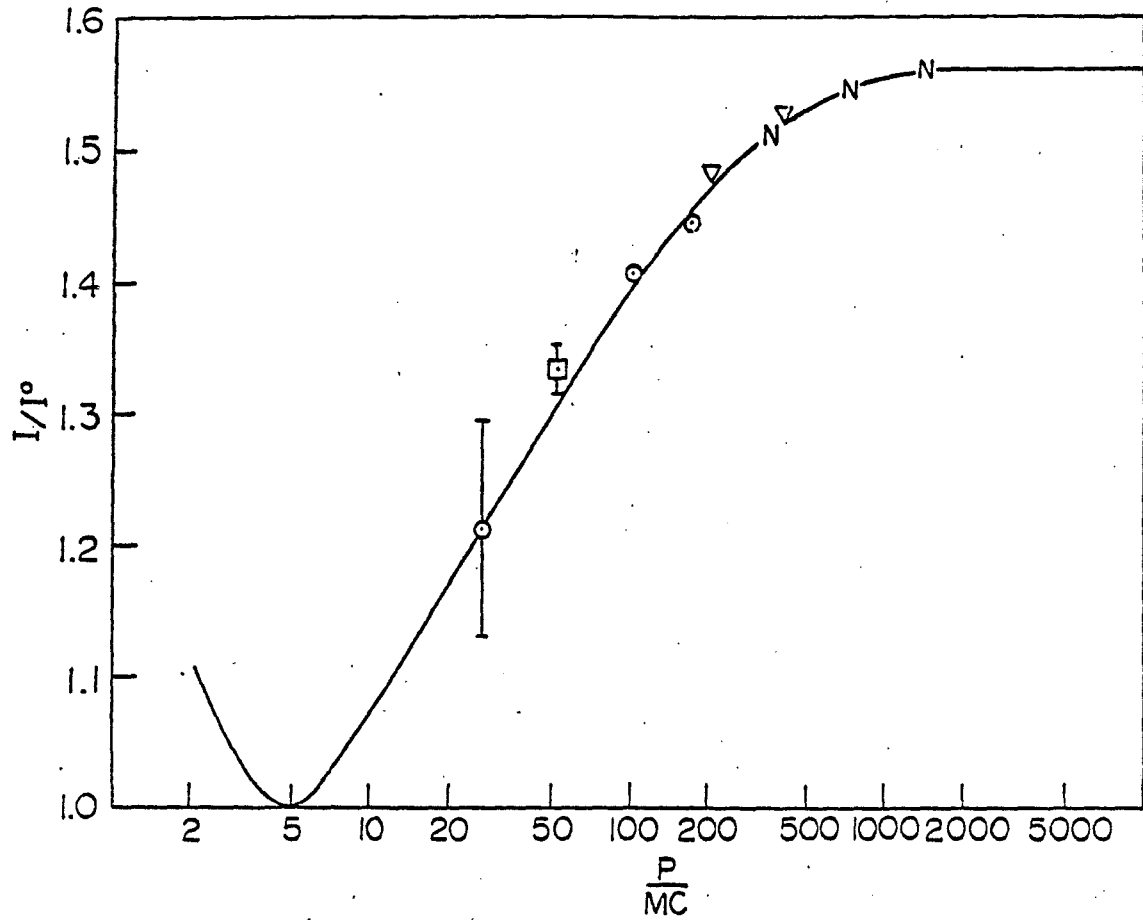


Fig. 2. Comparison of the ratio of average ionization to minimum average ionization with the theoretical curve from Ref. 9. The points,  $\circ$ , are normalized to the value for 100 GeV/c pions,  $\square$ , to 50 GeV/c pions, and  $\nabla$ , to 200 GeV/c pions (Ref. 11).

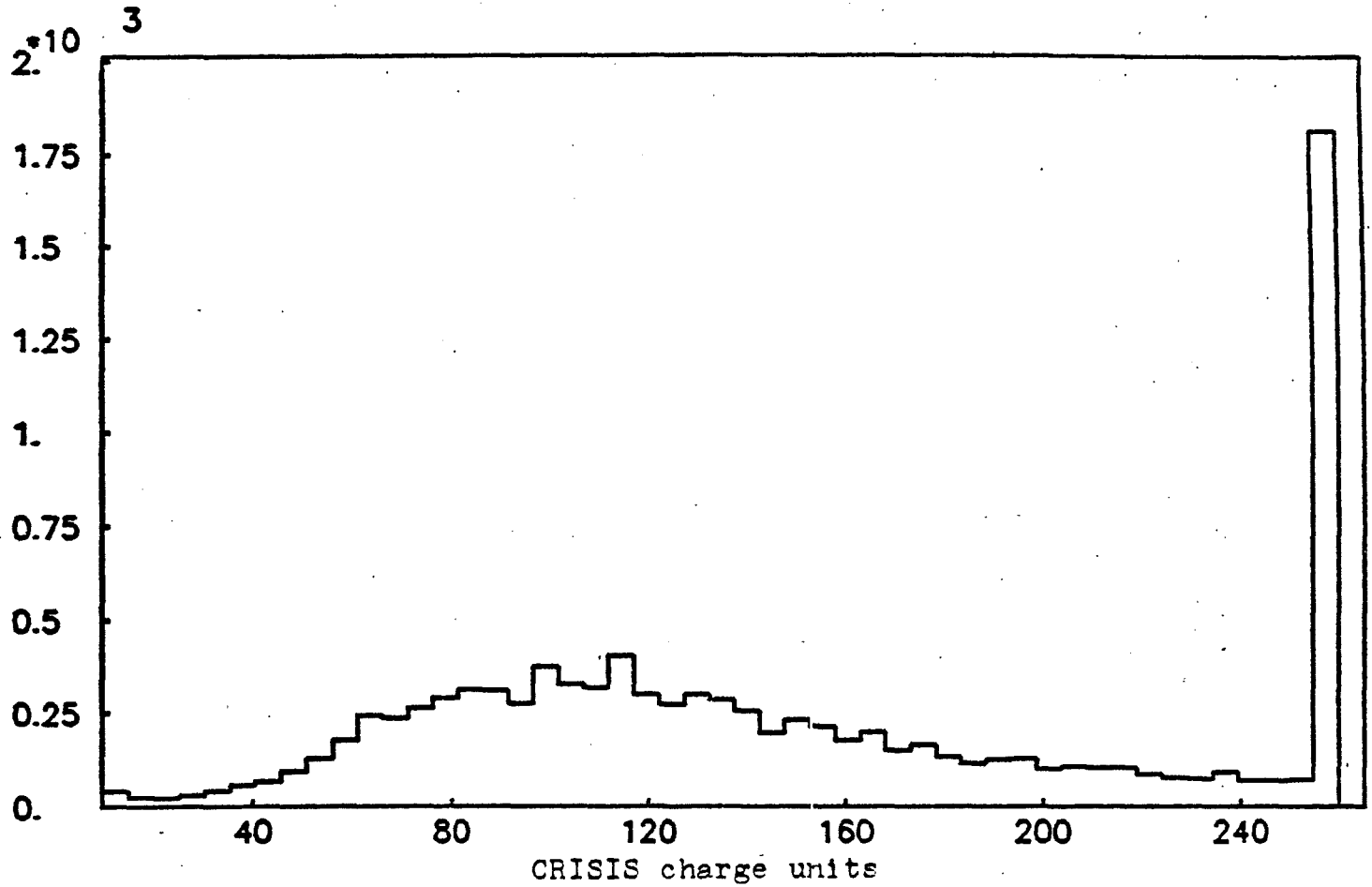


Fig. 3. Landau distribution obtained by using individual ionization samples from 200 GeV/c beams.

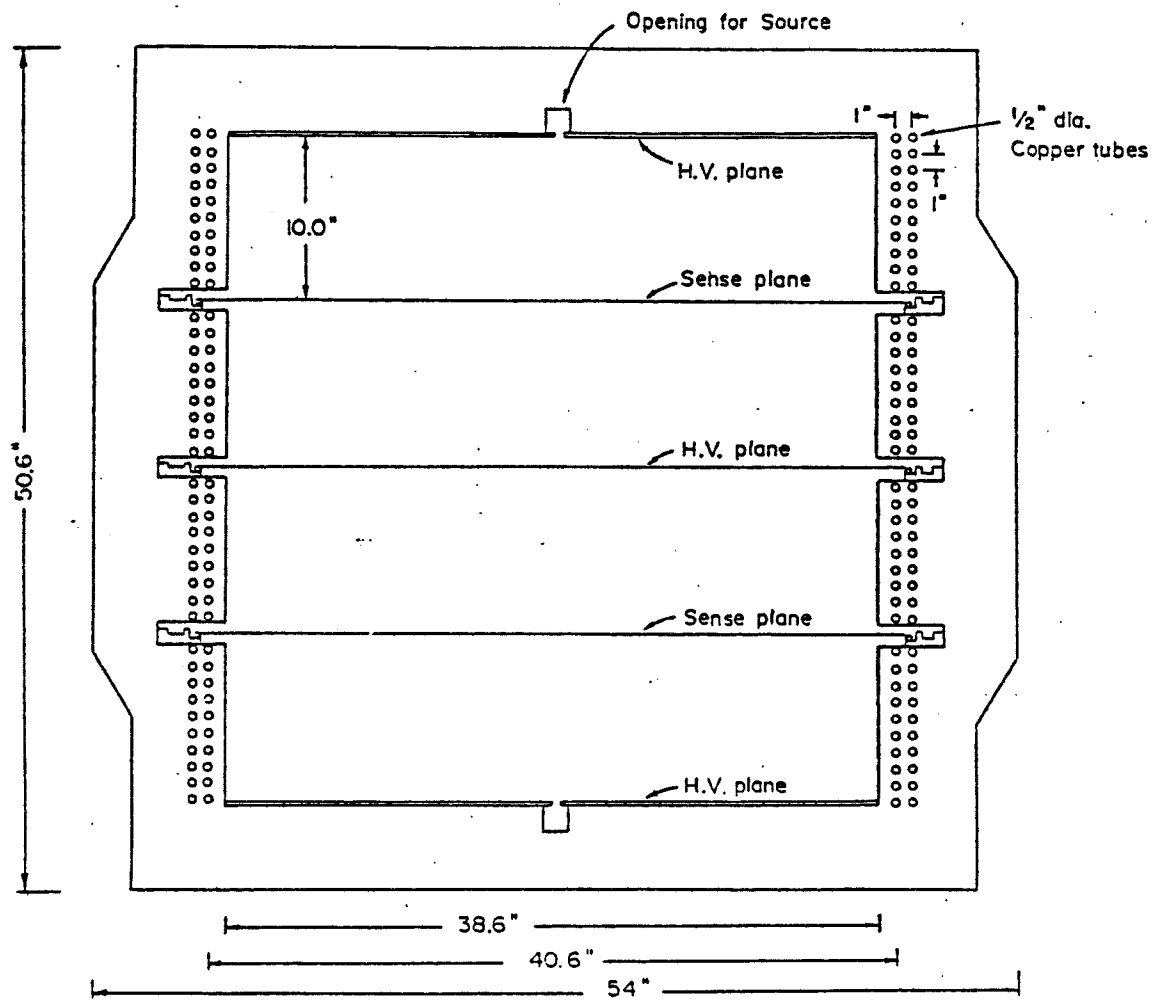


Fig. 4. Cross section of the CRISIS detector (Ref. 11).

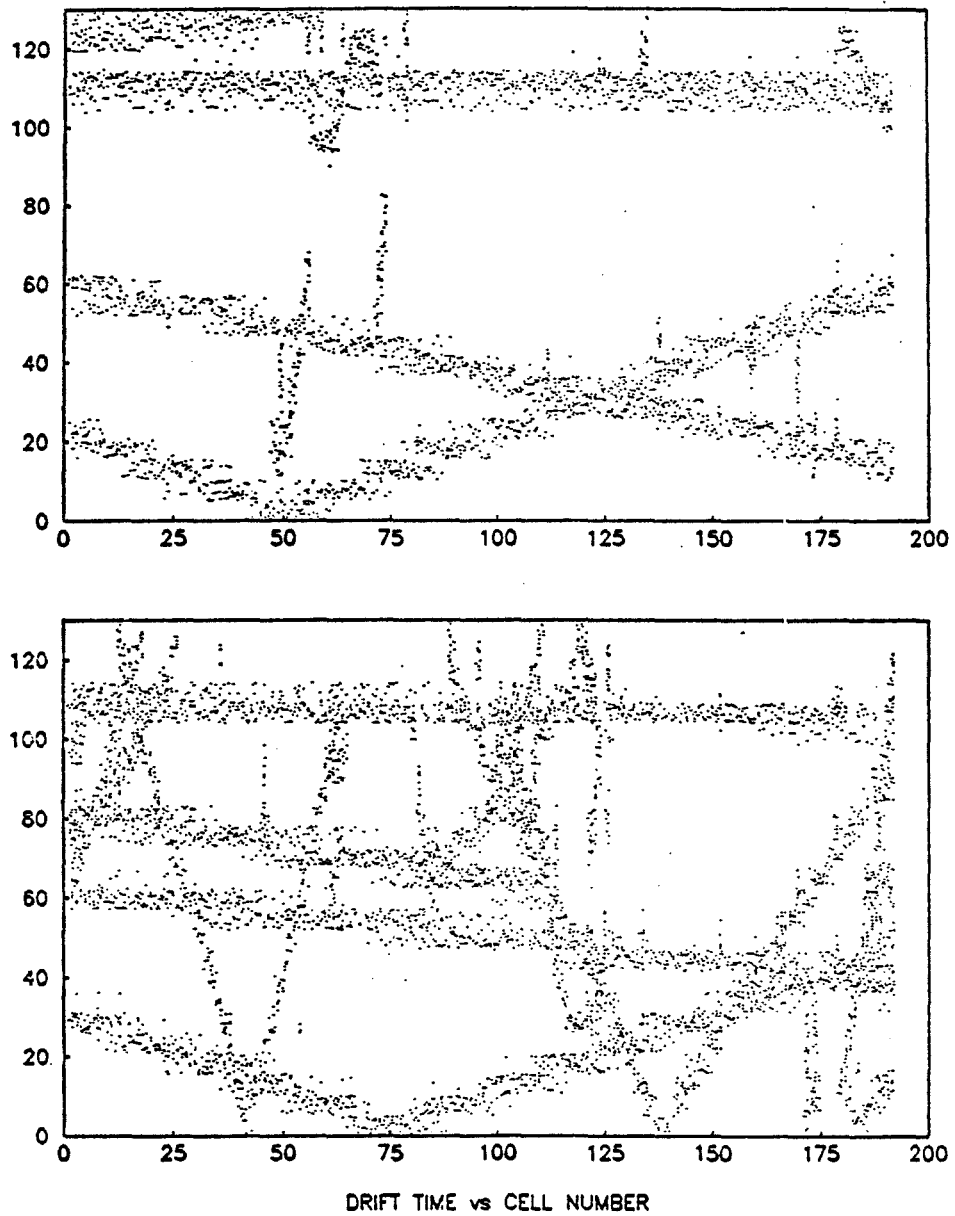


Fig. 5. Drift time in CRISIS time units (50 ns) versus cell number for two typical frames containing an interaction.

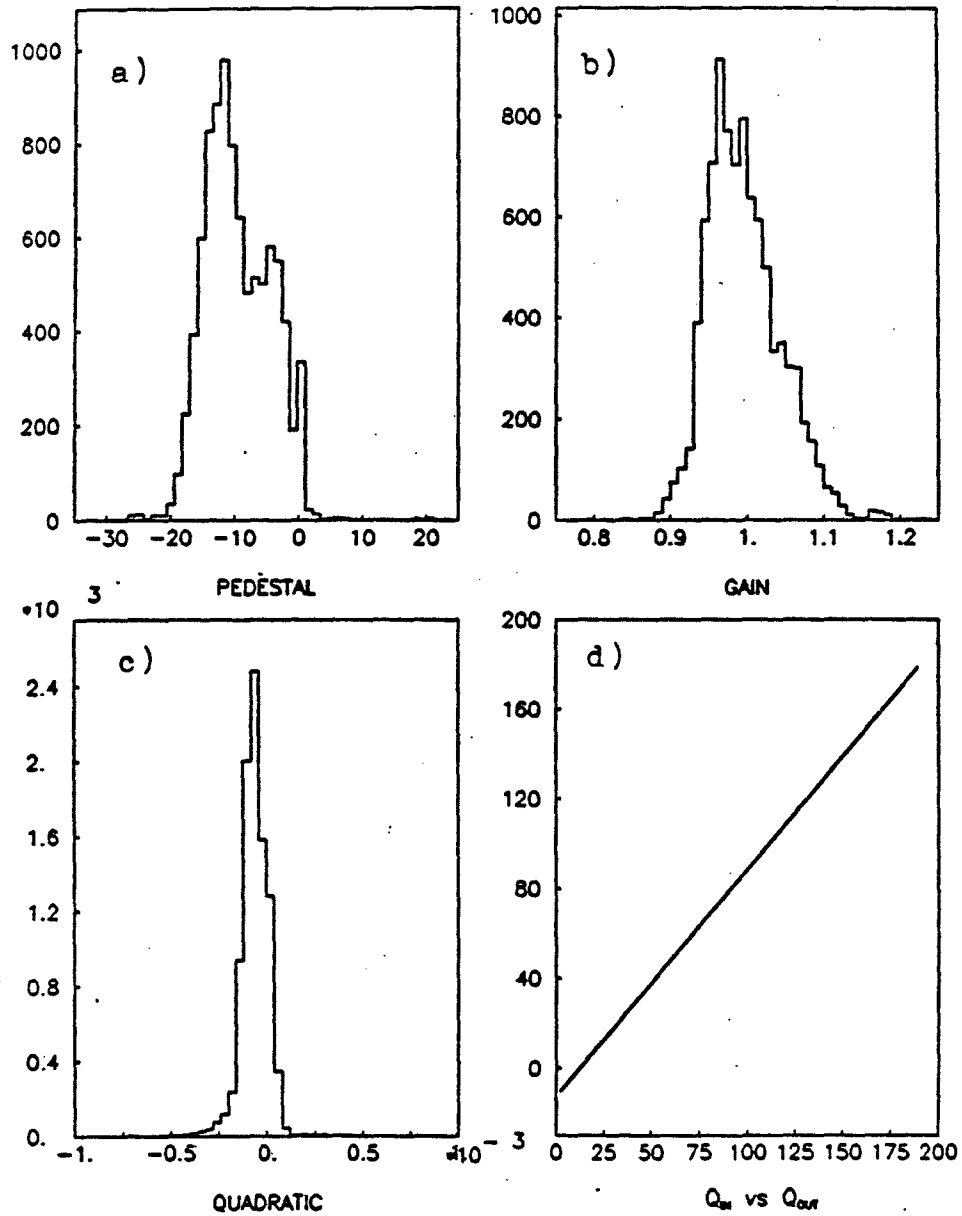


Fig. 6. a-c) Pedestal, gain and quadratic distributions for the 9216 CRISIS capacitors obtained from the pulser data. d) Average effect on the charge after applying  $Q_{out} = P + GQ_{in} + SQ_{in}^2$ .

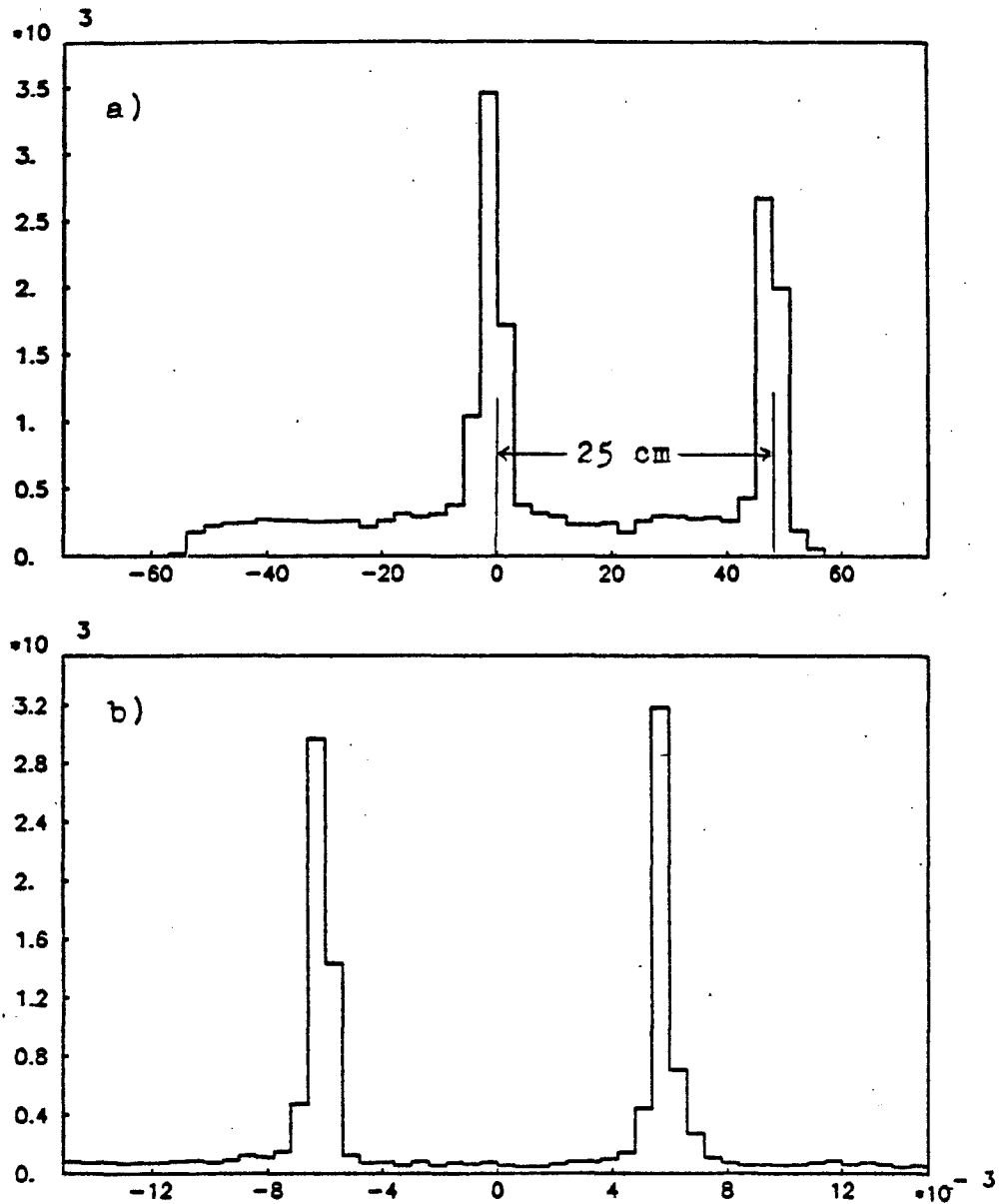


Fig. 7. a) Intercept and b) slope for all reconstructed CRISIS tracks. The double peaks result from the beams having a convergent slope in one of the CRISIS halves. Since every track has the ambiguity of being on either side of the sense plane, all tracks are assigned a divergent value.

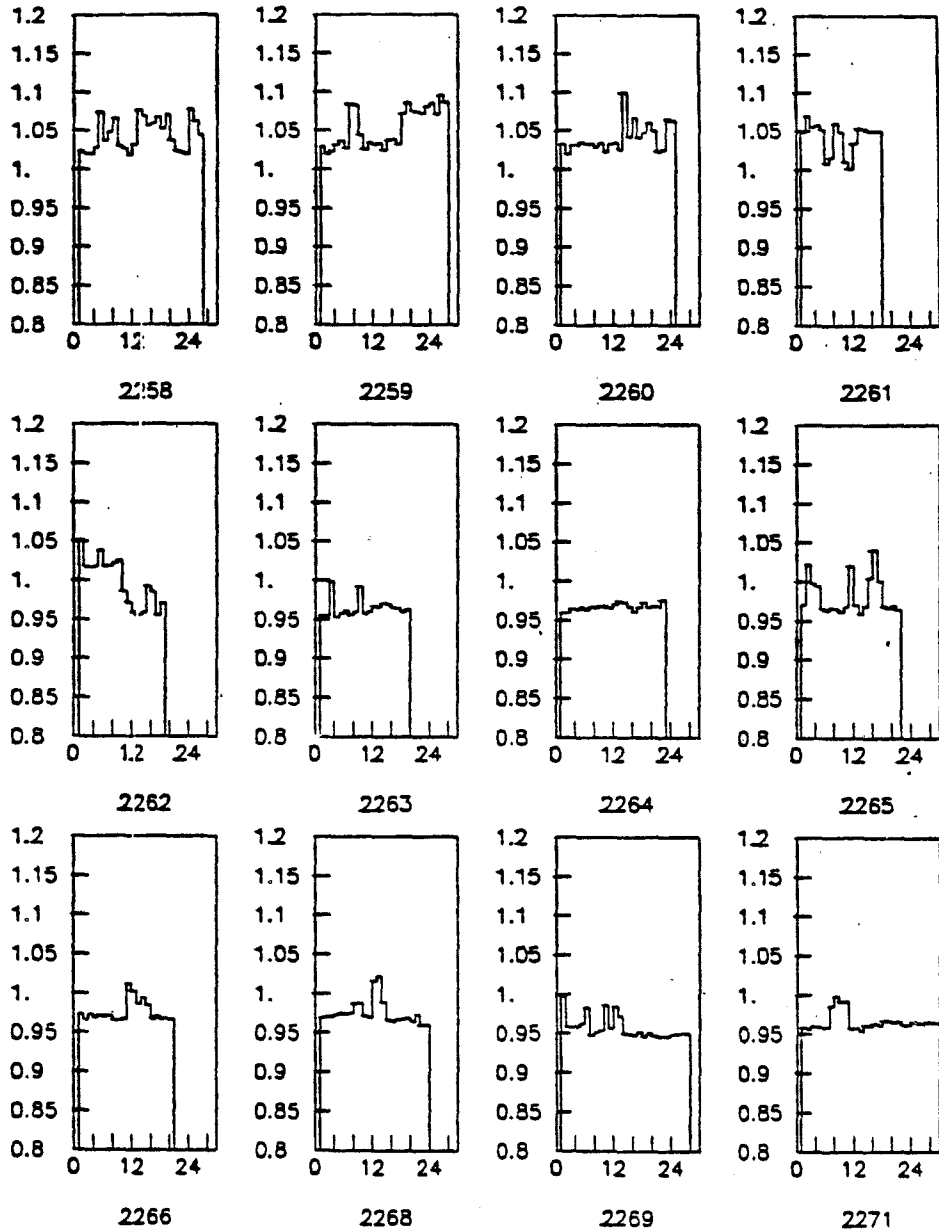


Fig. 8. Overall gain variation for several rolls. Each roll contains about 3000 frames or 3 hours of data-taking time.

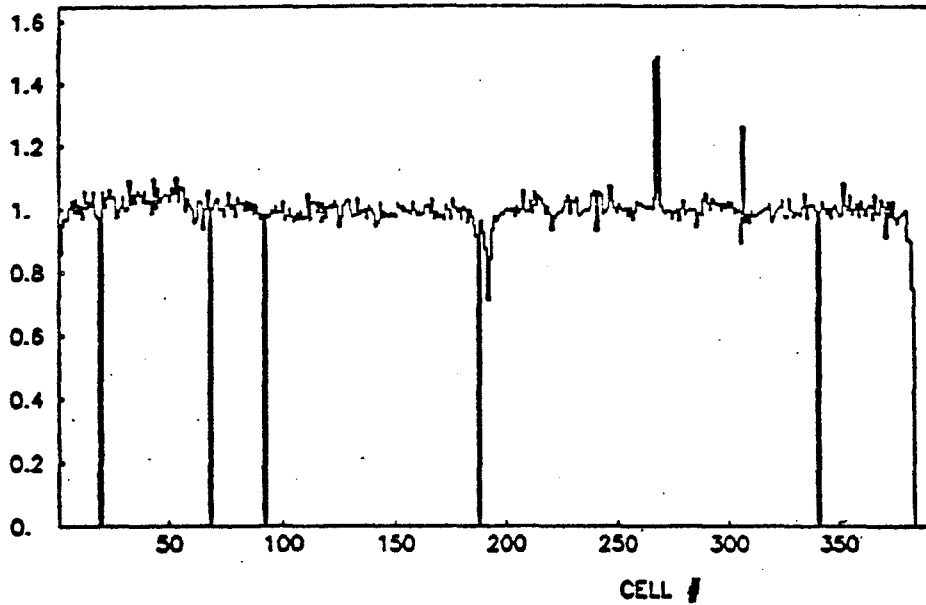


Fig. 9. Cell-to-cell variation.

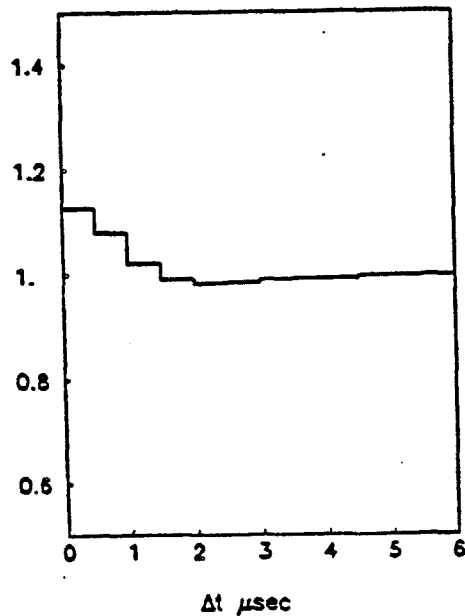


Fig. 10. Rate correction.  
 $\Delta t$  is the difference in time between the arrival at the sense wire of a charge for which the correction is to be made, and a preceding charge.

$Q_{out}$	Raw charges stored in the CRISIS electronics
$Q_{out} = P + GQ + SQ^2$	Calculate $Q$ using the pulser coefficients
$Q = \bar{G}Q$	Correct for the overall gain variation
$Q^i = C^i Q^i$	Correct for the cell-to-cell variation
$Q = RQ$	Correct for the rate effect
$\Sigma Q = \bar{I}$	Throw away any $Q < 30$
	Keep the lowest 70% of the charges
	Calculate the average ionization $\bar{I}$ .
$\bar{I} \rightarrow$ particle identification	Combine the ionization, charge and momentum of the particle with the beam information to assign a probability that the particle is a pion, kaon or proton

Fig. 11. Corrections made on the CRISIS raw charges leading to a particle's identification.

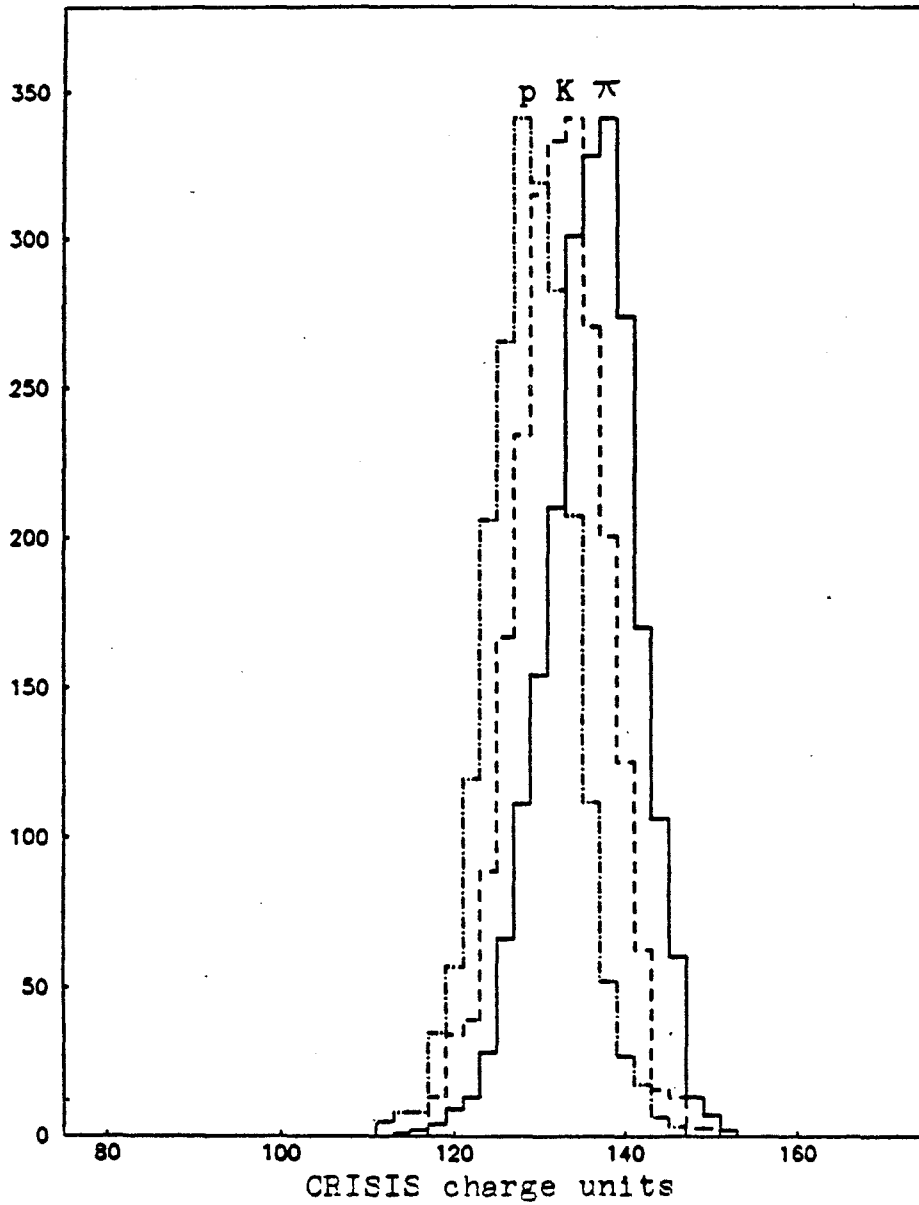


Fig. 12. Separation of pion, kaon and proton beams at 200 GeV/c momentum.

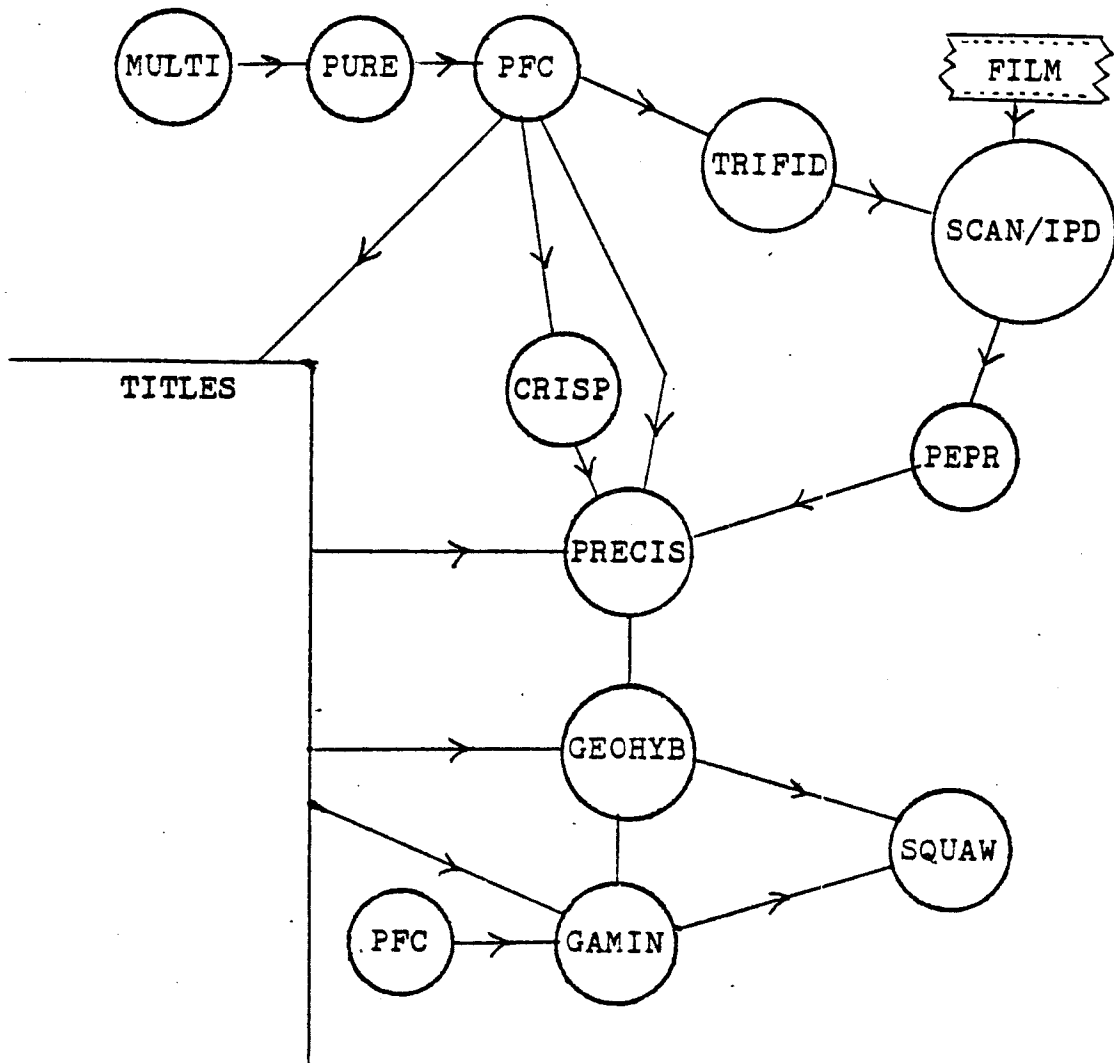


Fig. 13. E565/570 software logic.

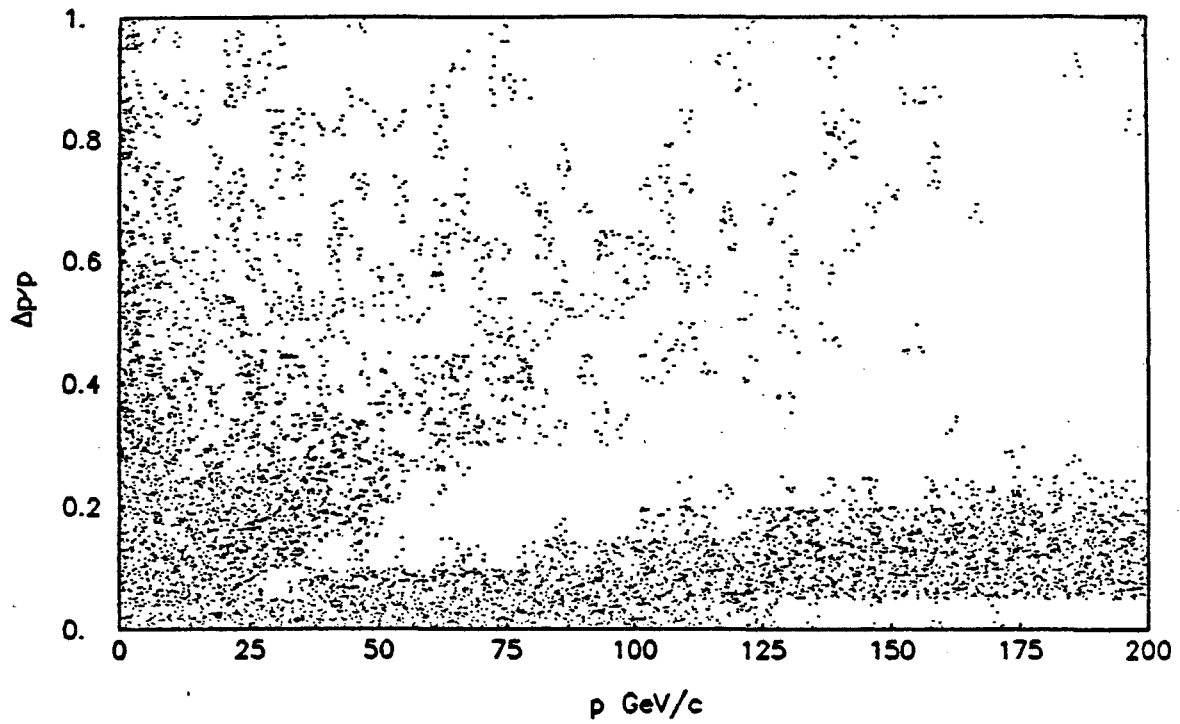


Fig. 14. Momentum resolution of all the secondaries. The lower band corresponds to those tracks which were fully hybridized by the downstream spectrometer.

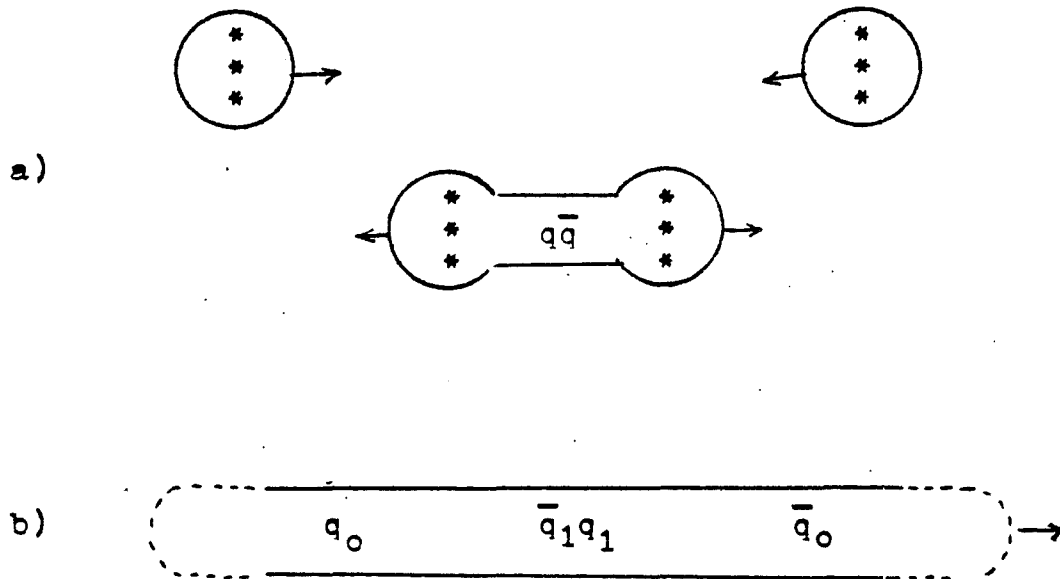


Fig. 15. a) For low  $Q^2$ , two "bags" can interact and produce a  $q\bar{q}$  pair out of the sea. The original valence quarks continue along their way without further affecting the fragmentation process in the central region. b) A  $q_1\bar{q}_1$  pair produced in a linear force field between quarks  $q_0$  and  $\bar{q}_0$ .

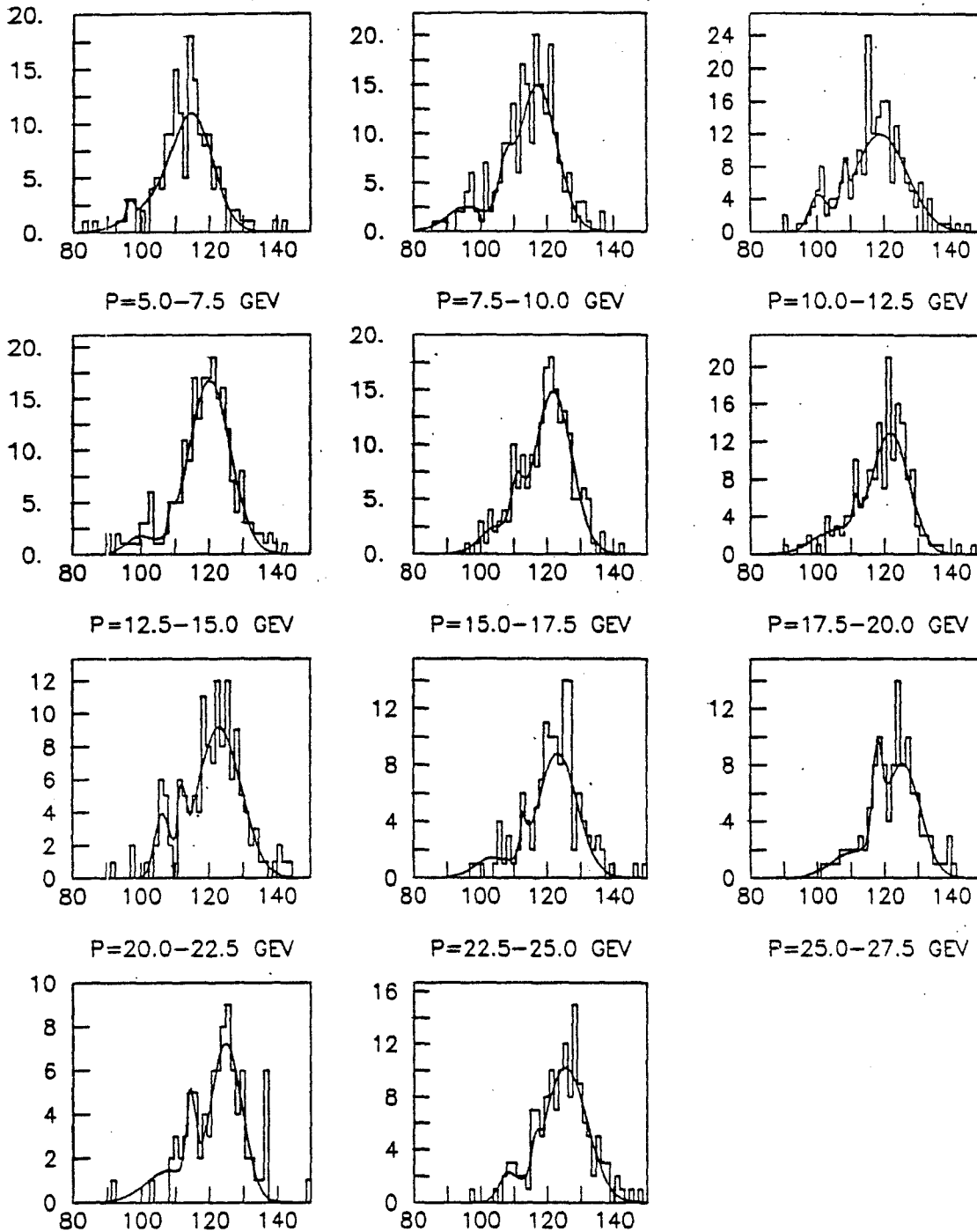


Fig. 16. Average ionization of the CRISIS tracks for each 2.5 GeV/c momentum interval. The curves represent a 9 parameter least squares fit corresponding to three gaussian distributions.

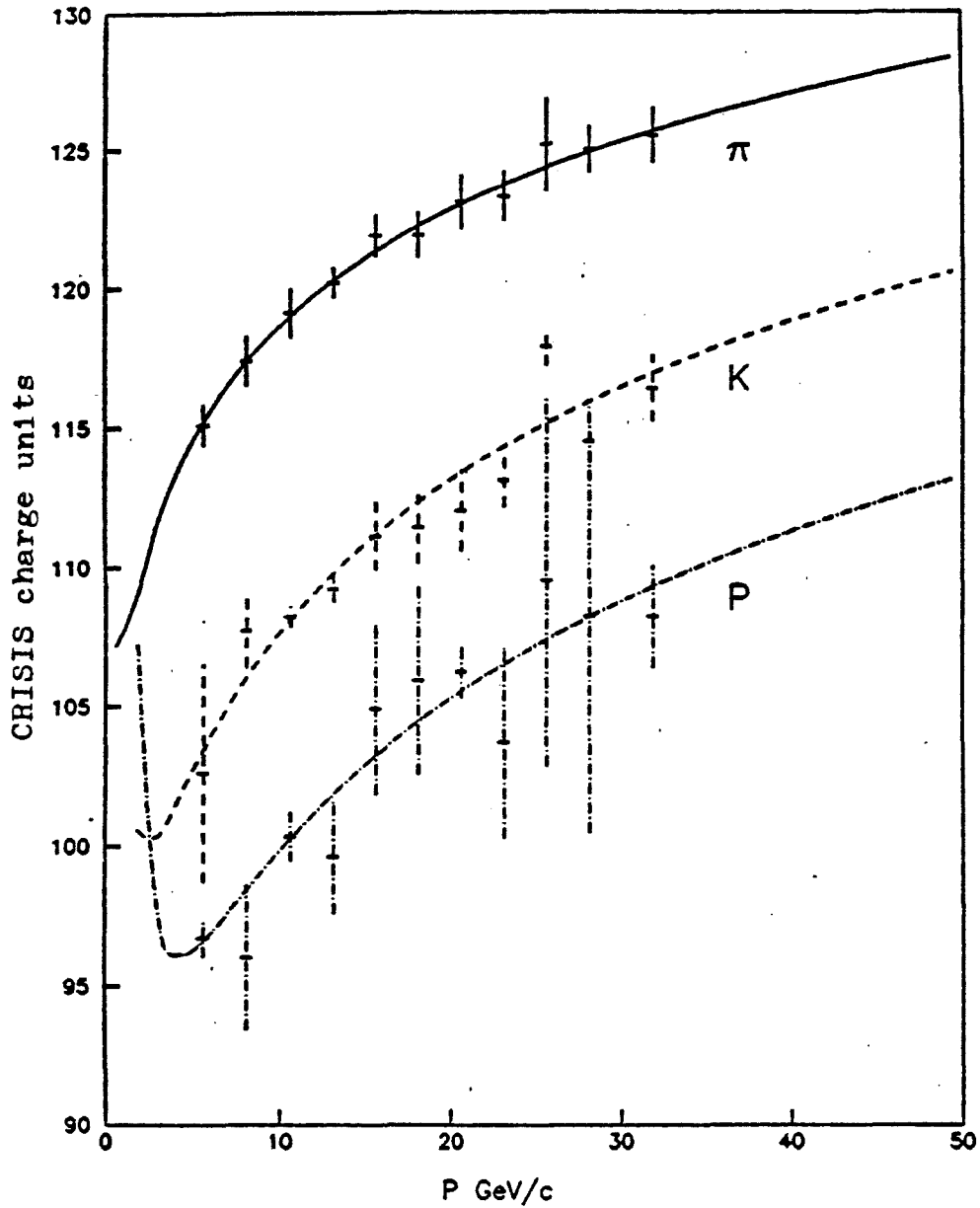


Fig. 17. Separation of pions, kaons and protons by CRISIS. The data points are the centers of the gaussian fits to the average ionizations (Fig. 16).

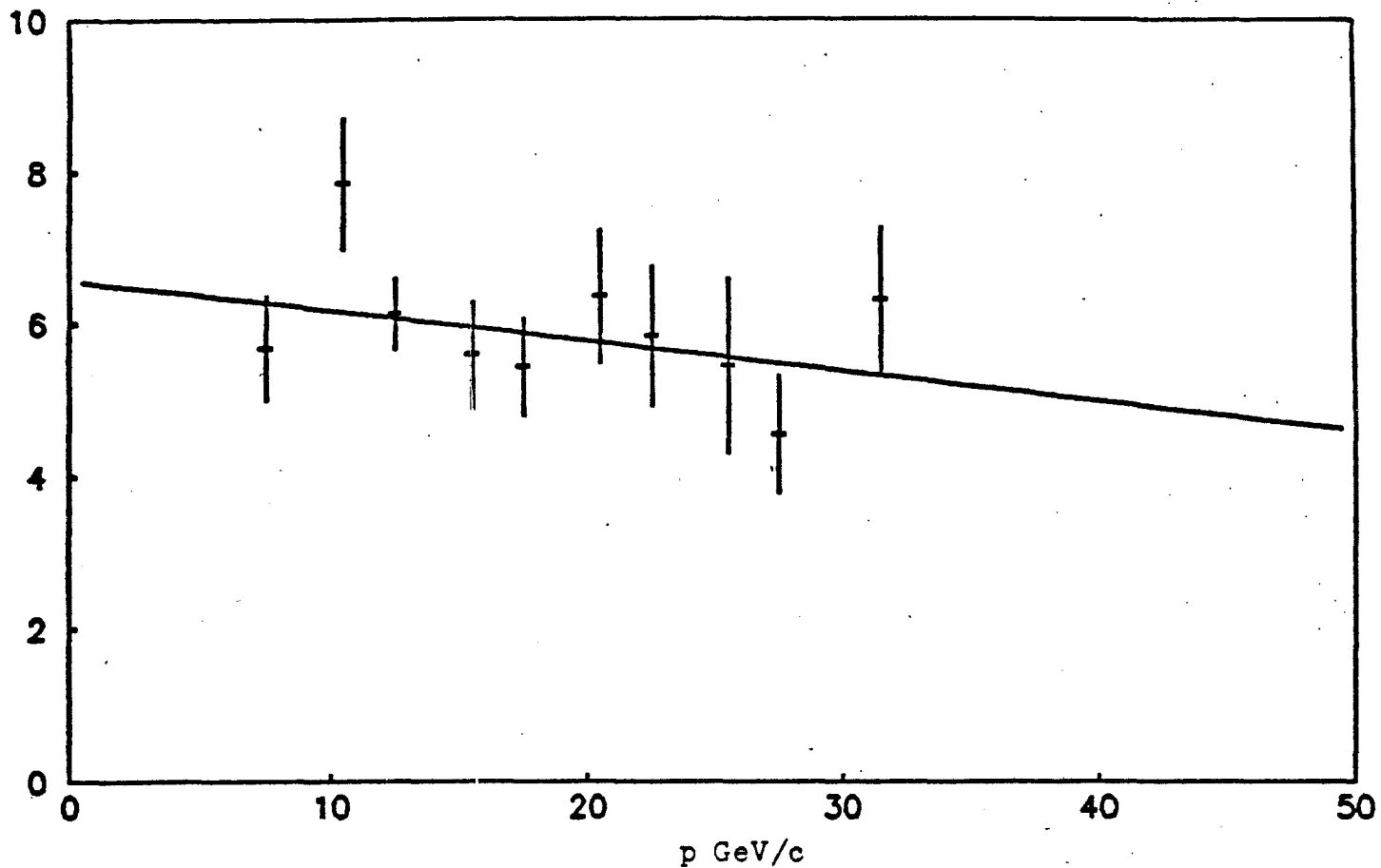


Fig. 18. Width  $\sigma$  (in CRISIS charge units) of the pion ionization distributions as a function of momentum.

## VERTEX COORDINATE DISTRIBUTIONS

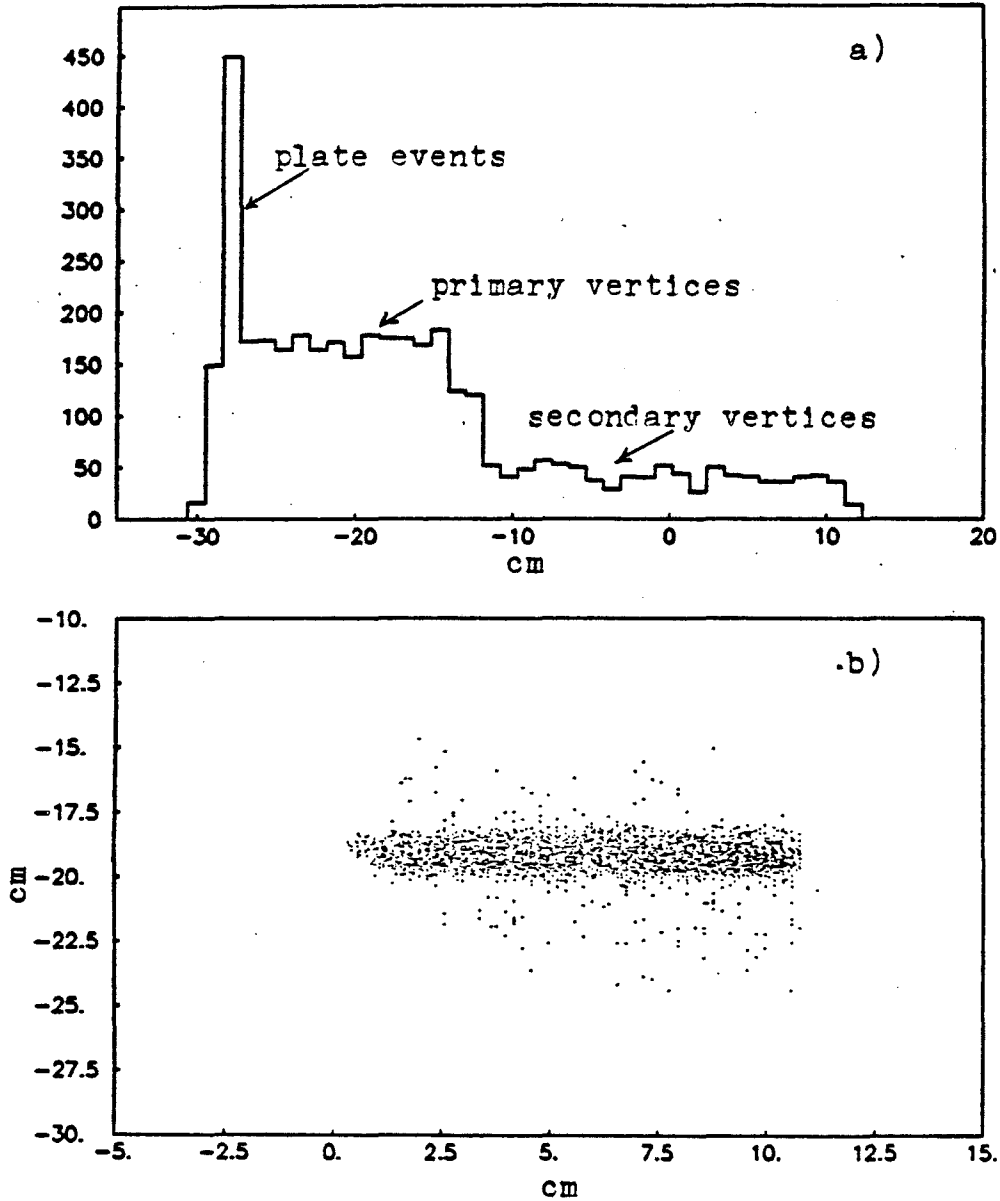


Fig. 19. a) Distribution of the vertices in the bubble chamber along the beam direction. b) Beam profile.

## LUND MODEL INCLUSIVE PARTICLE PRODUCTION

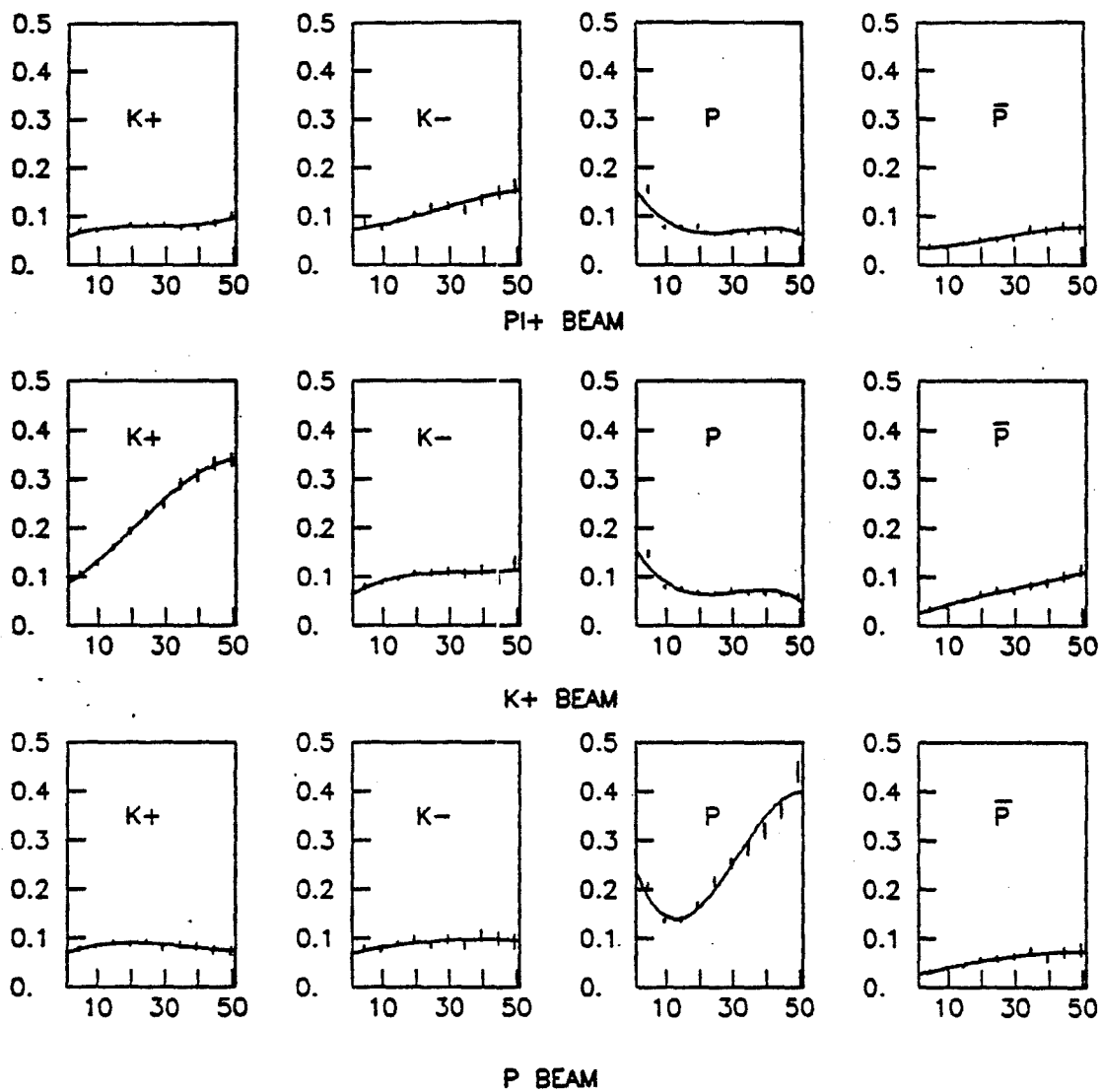


Fig. 20. RATIO (PARTICLE/ALL PARTICLES OF THE SAME CHARGE GOING THROUGH CRISIS) VS  $P$  (GEV/C)

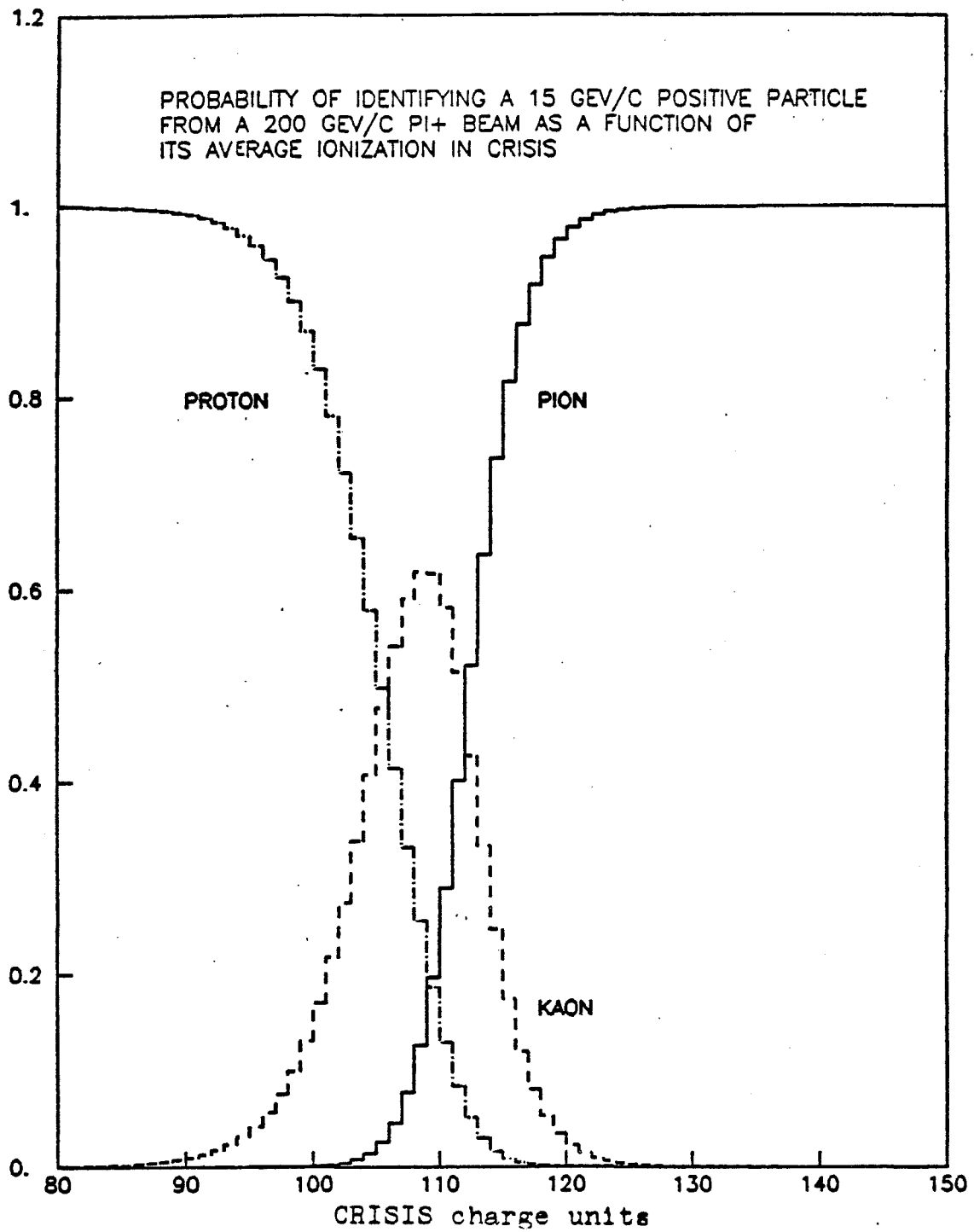


Fig. 21

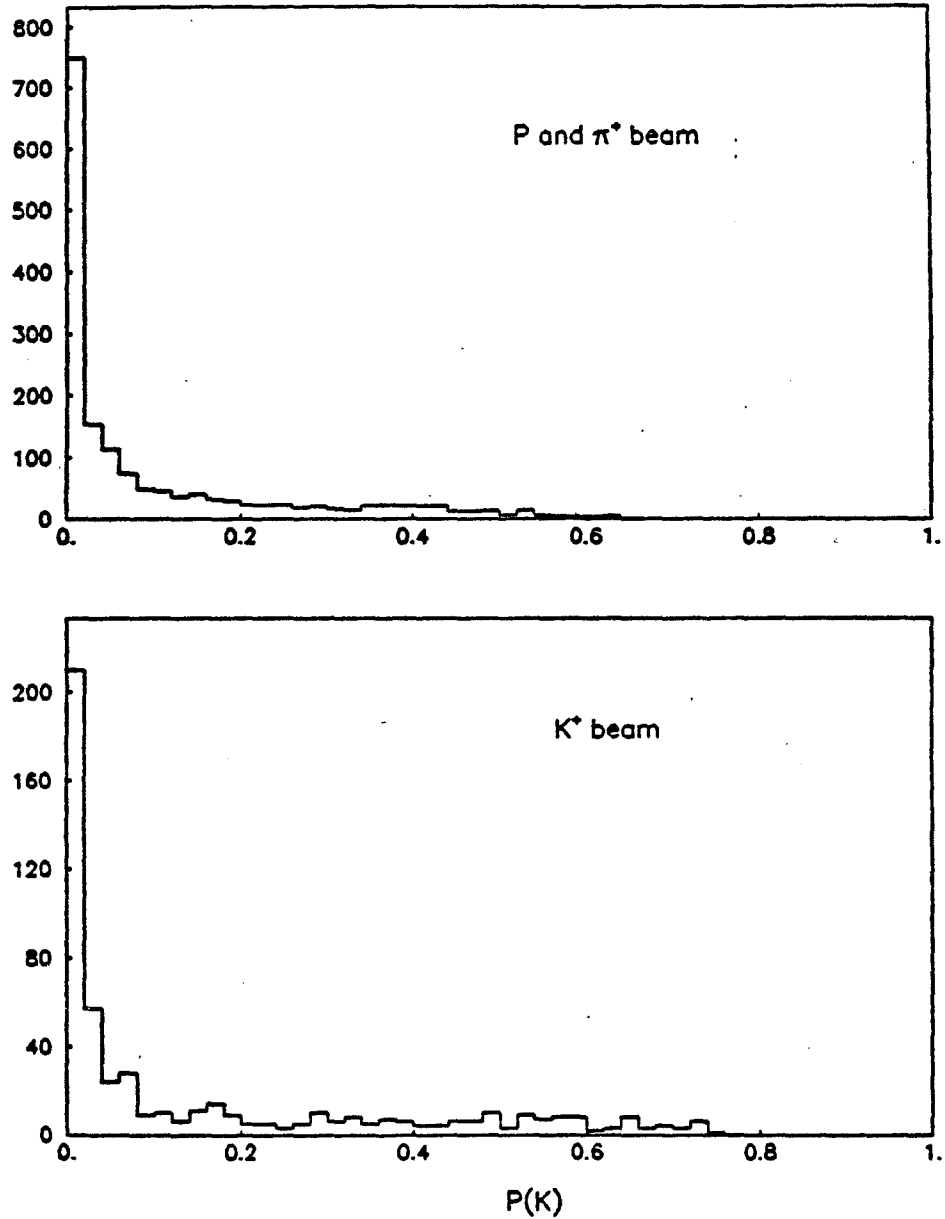


Fig. 22. Probability of particles in CRISIS to be kaons. Each entry corresponds to a single CRISIS track.

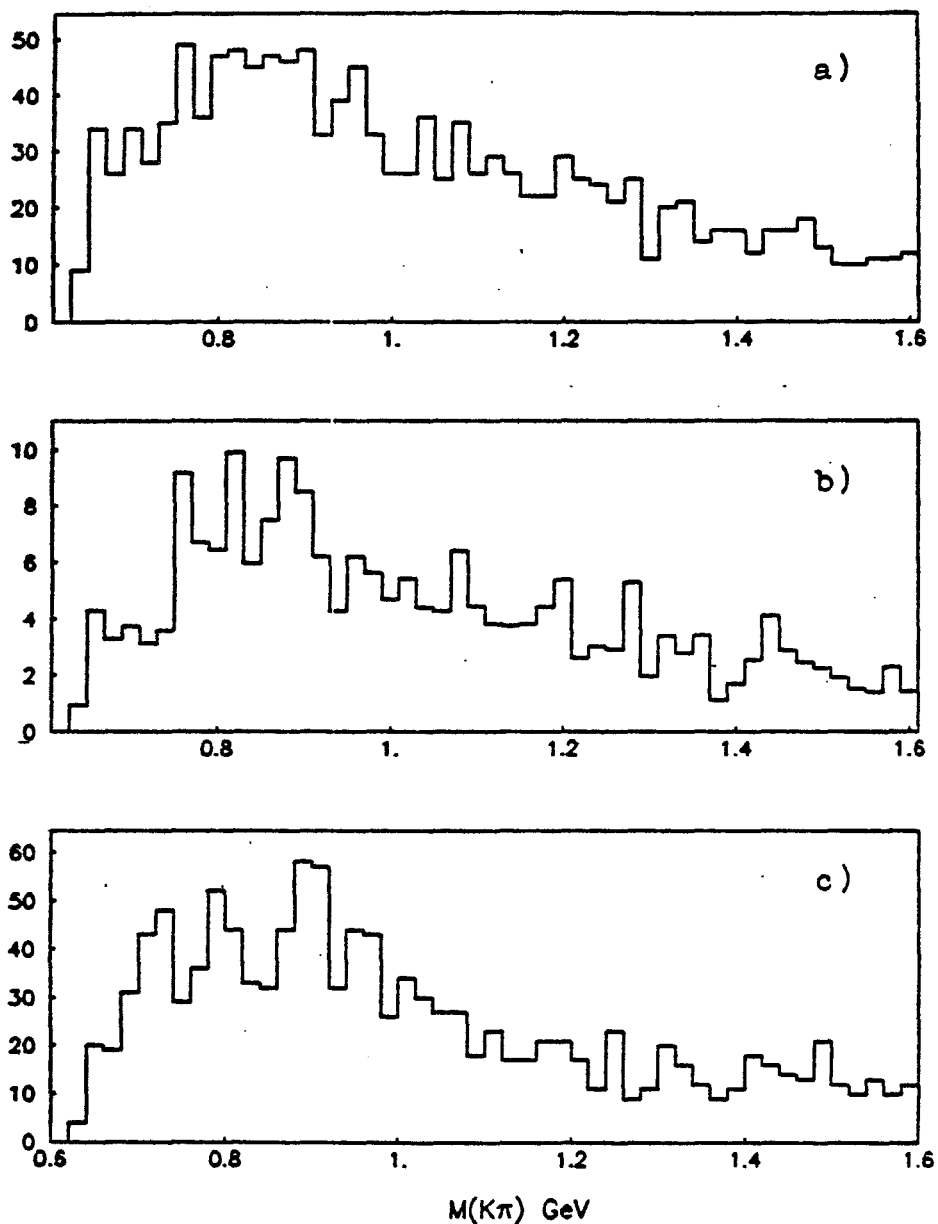


Fig. 23. Invariant mass  $M(K^{\pm}\pi^{\mp})$  distributions. a) Every track in CRISIS is assumed to be a kaon. b) Each entry is weighted by the probability that the track is a kaon. c) Lund Model simulation with only those kaons used which would have gone through CRISIS.

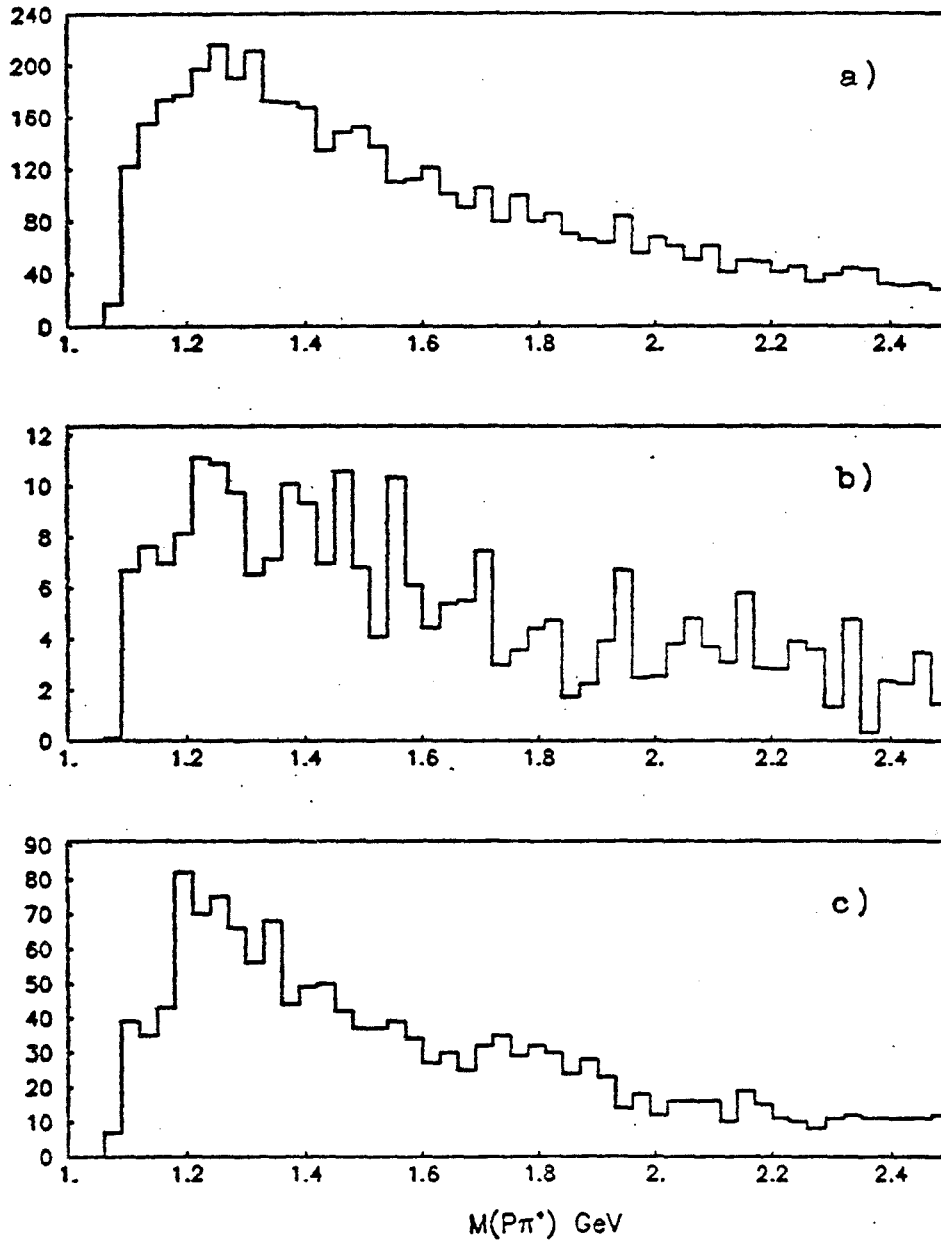


Fig. 24. Invariant mass  $M(p\pi^+)$  distributions. a) Every positive track in CRISIS is assumed to be a proton. b) Each entry is weighted by the probability that the track is a proton. c) Lund Model simulation with only those protons used which would have gone through CRISIS.

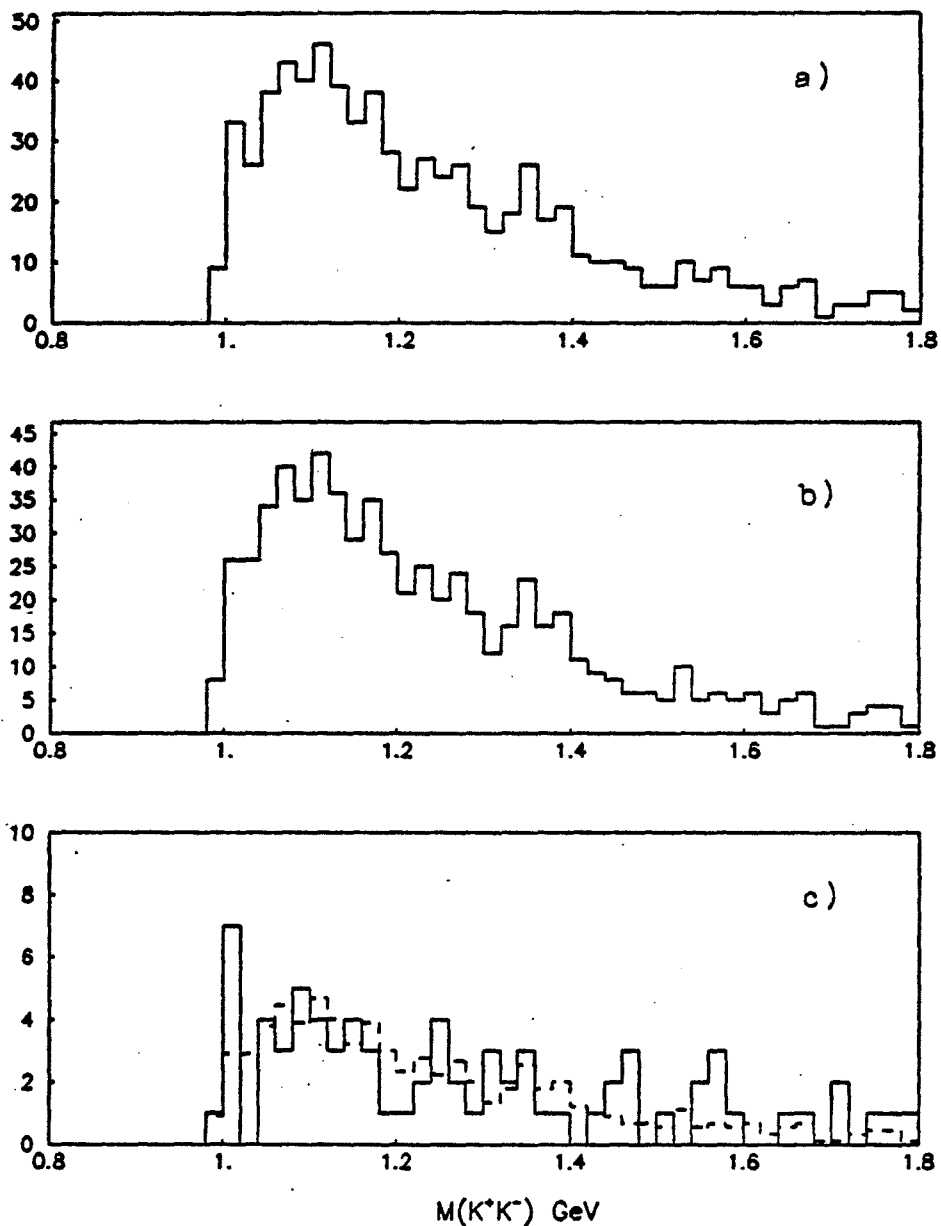


Fig. 25. Invariant mass  $M(K^+K^-)$  distributions. a) All tracks in CRISIS are assumed to be kaons. b) Each entry is weighted by the probability that both particles are not kaons. c) Each entry is weighted by the probability that both tracks are kaons (solid lines). Superimposed (broken lines) is  $\bar{b}$ ) normalized to the contents of c).

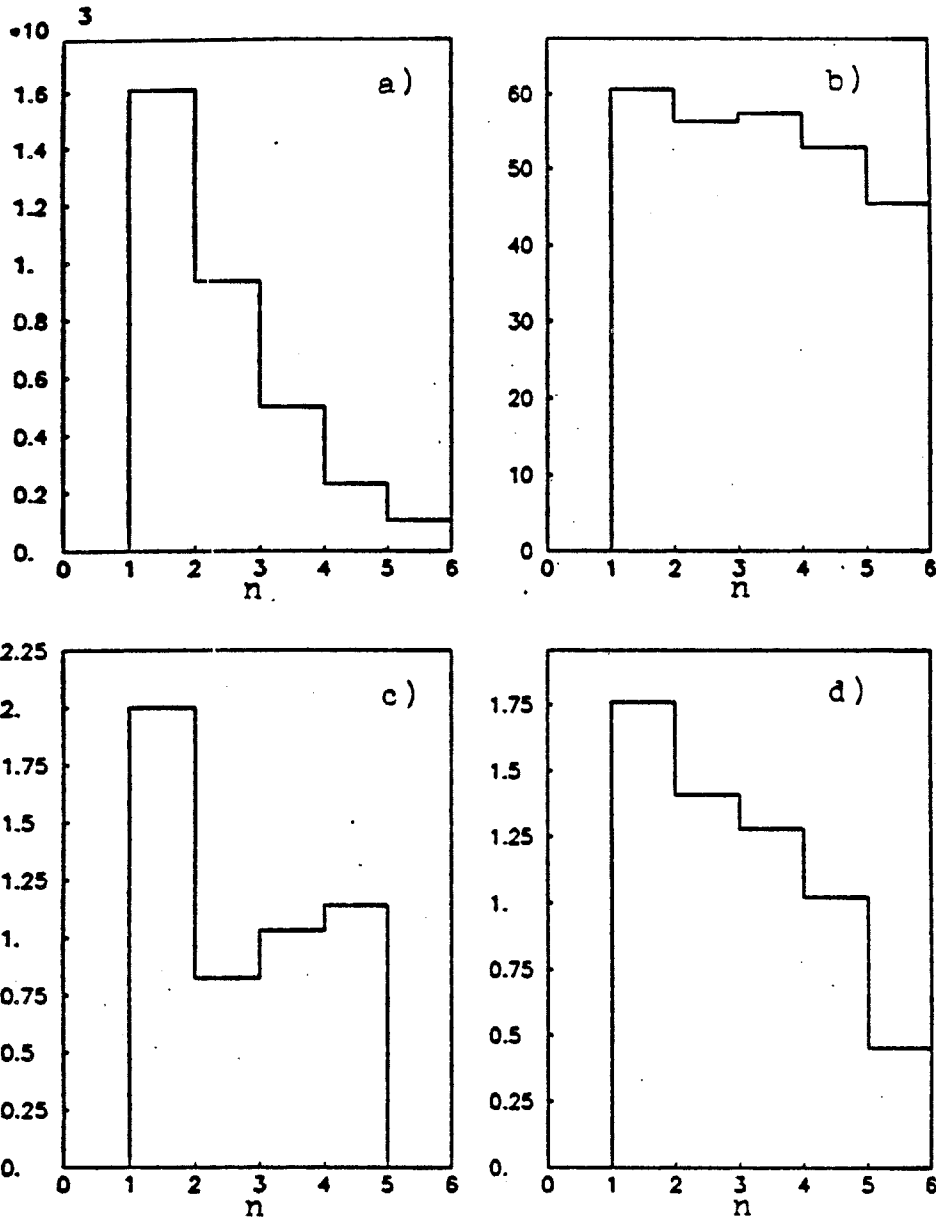


Fig. 26.  $n$  distributions for  $\pi^+ p$  and  $pp$  events. a) All pairs of particles in CRISIS (background). b)  $+ -$  pairs in CRISIS after normalization by the background. c)  $K^+K^-$  pairs in CRISIS after normalization. d) Same as c), as simulated by the Lund Model.

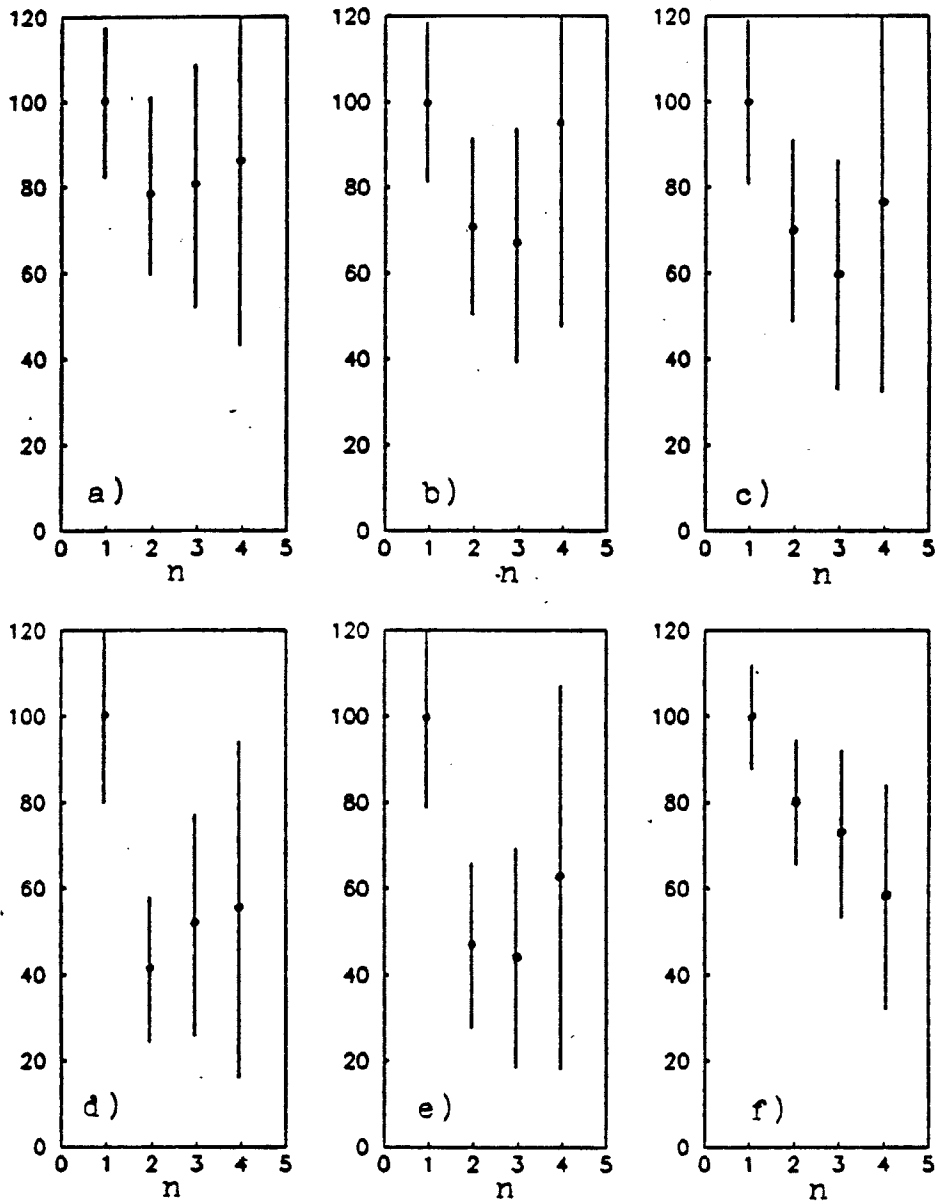


Fig. 27.  $n$  distributions for  $K^+K^-$  pairs produced in  $pp$  and  $\pi^+p$  interactions. The probability that each track is a kaon is greater than a) 5%, b) 10%, c) 15%, d) 20%, e) 25%, f) 30%. In each case the first bin is normalized to 100.

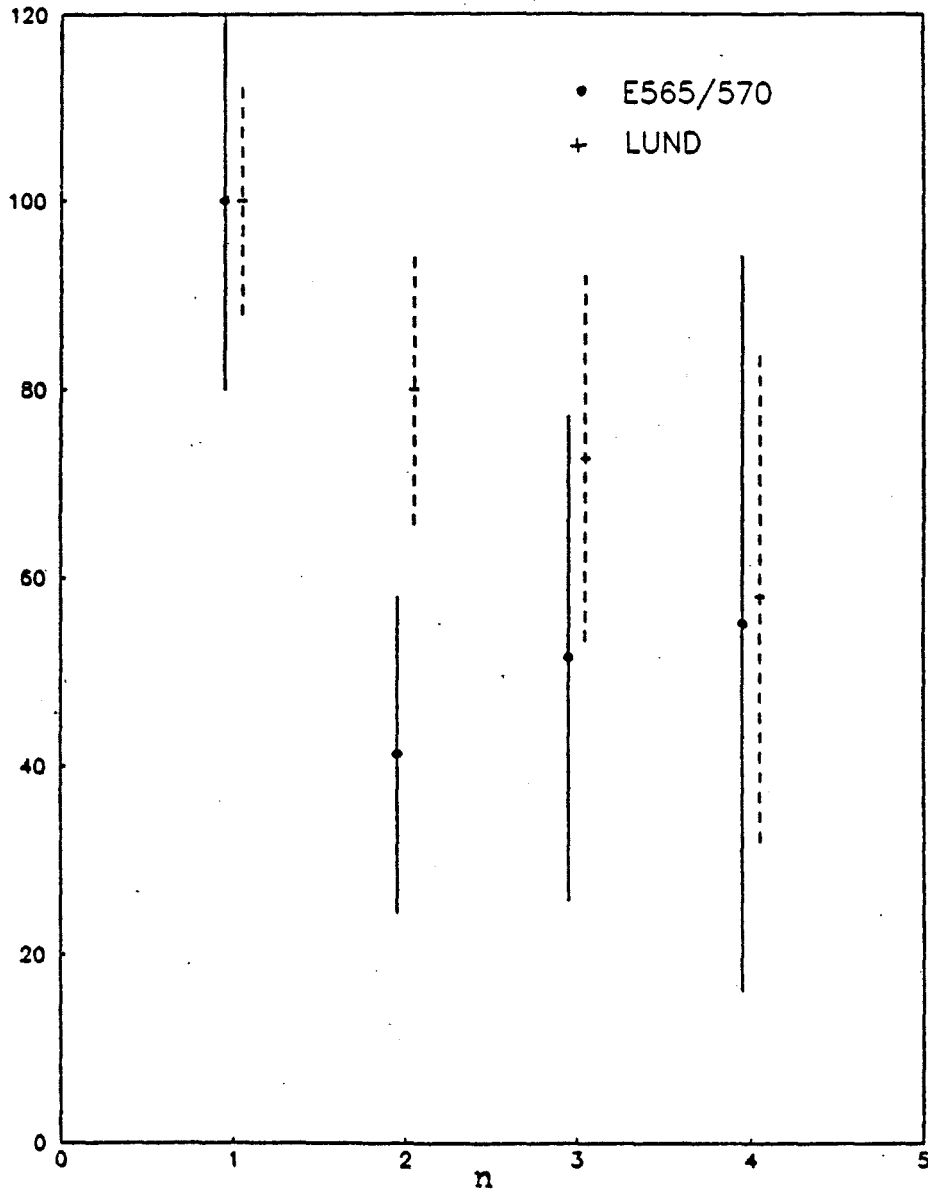


Fig. 28.  $n$  distribution for  $K^+K^-$  pairs in CRISIS using pion and proton beams only. Each entry for the data is weighted by the probability that both particles are kaons.

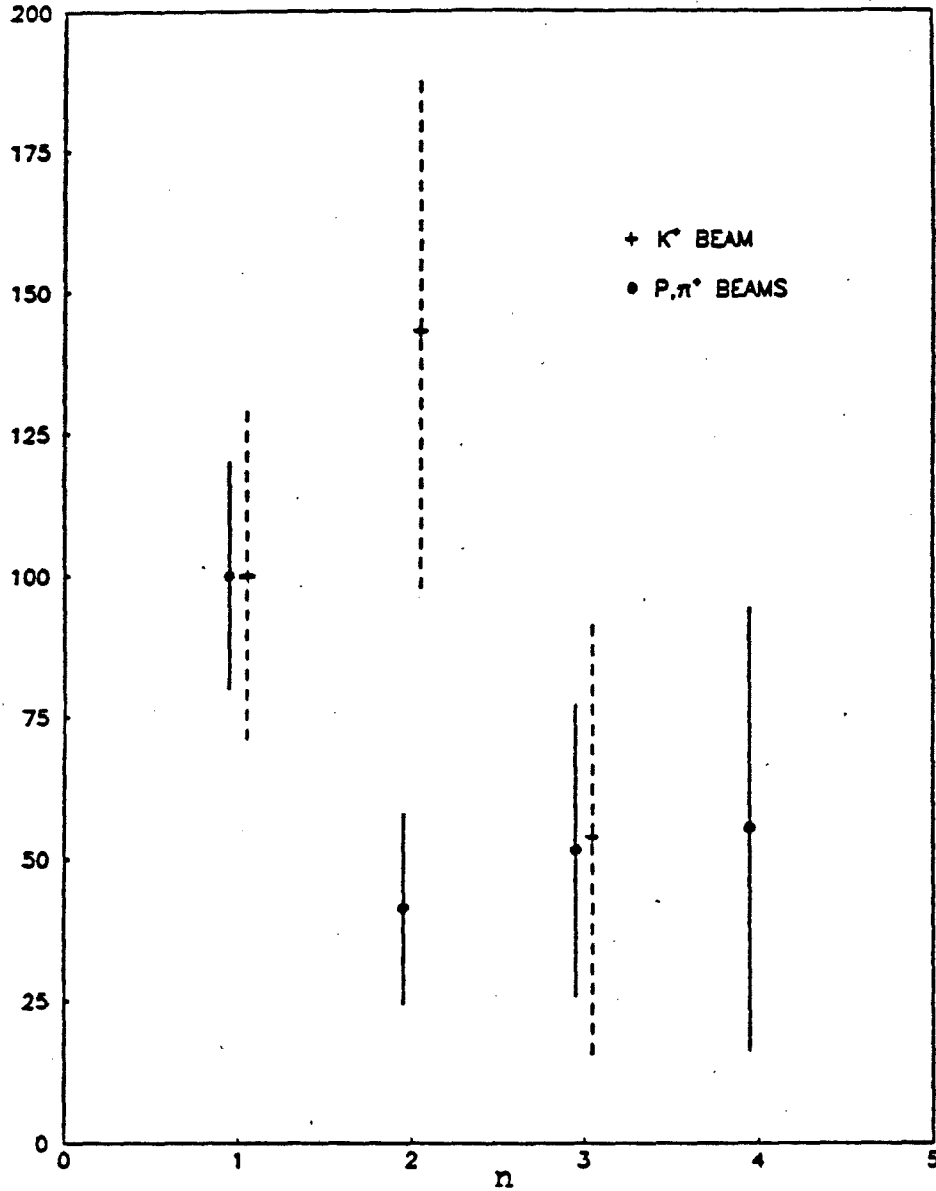


Fig. 29.  $n$  distribution for  $K^+K^-$  pairs in CRISIS. Each entry is weighted by the probability that both particles are kaons.

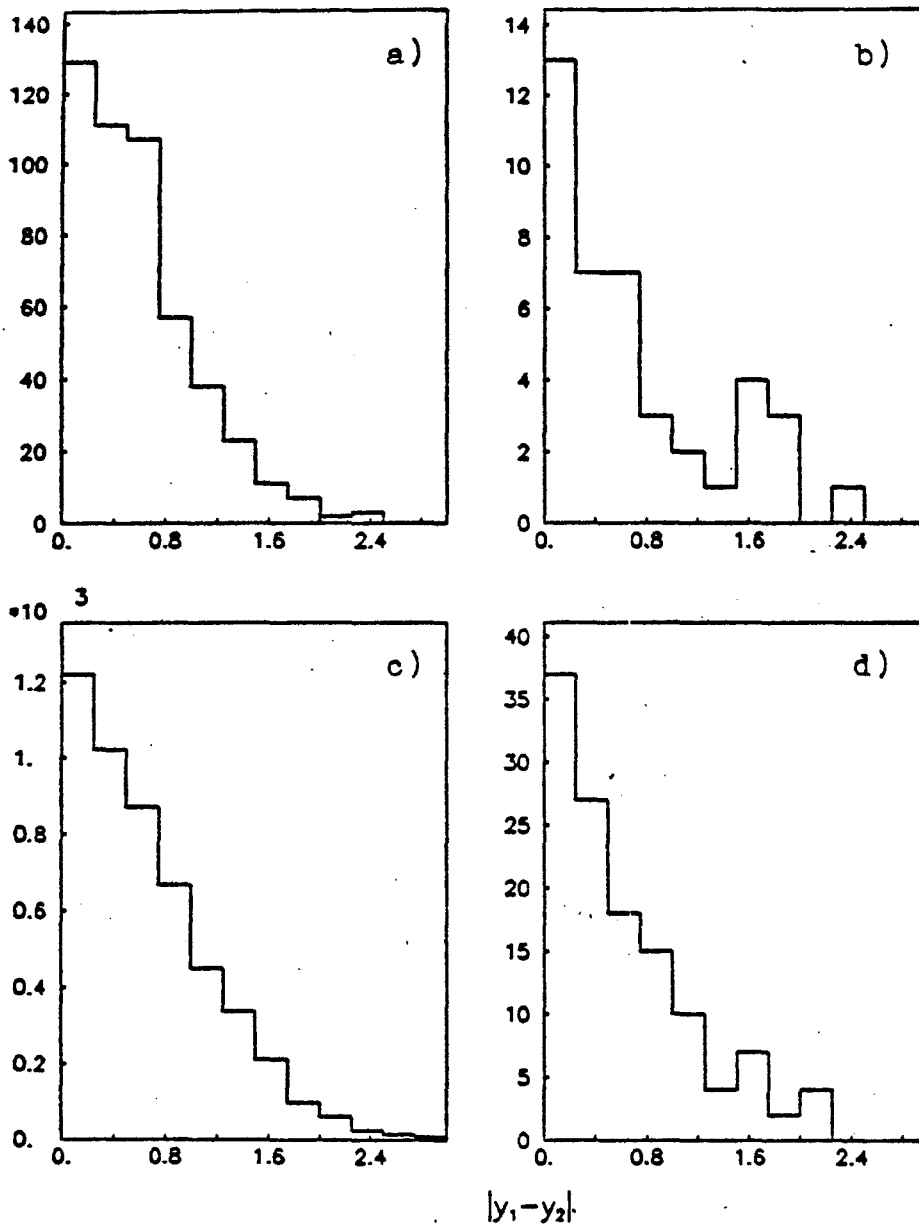


Fig. 30. Difference in rapidity between a) all pairs of particles in CRISIS and b)  $K^+K^-$  pairs in CRISIS using pion and proton beams only. c-d) Lund Model simulation of a) and b) respectively.

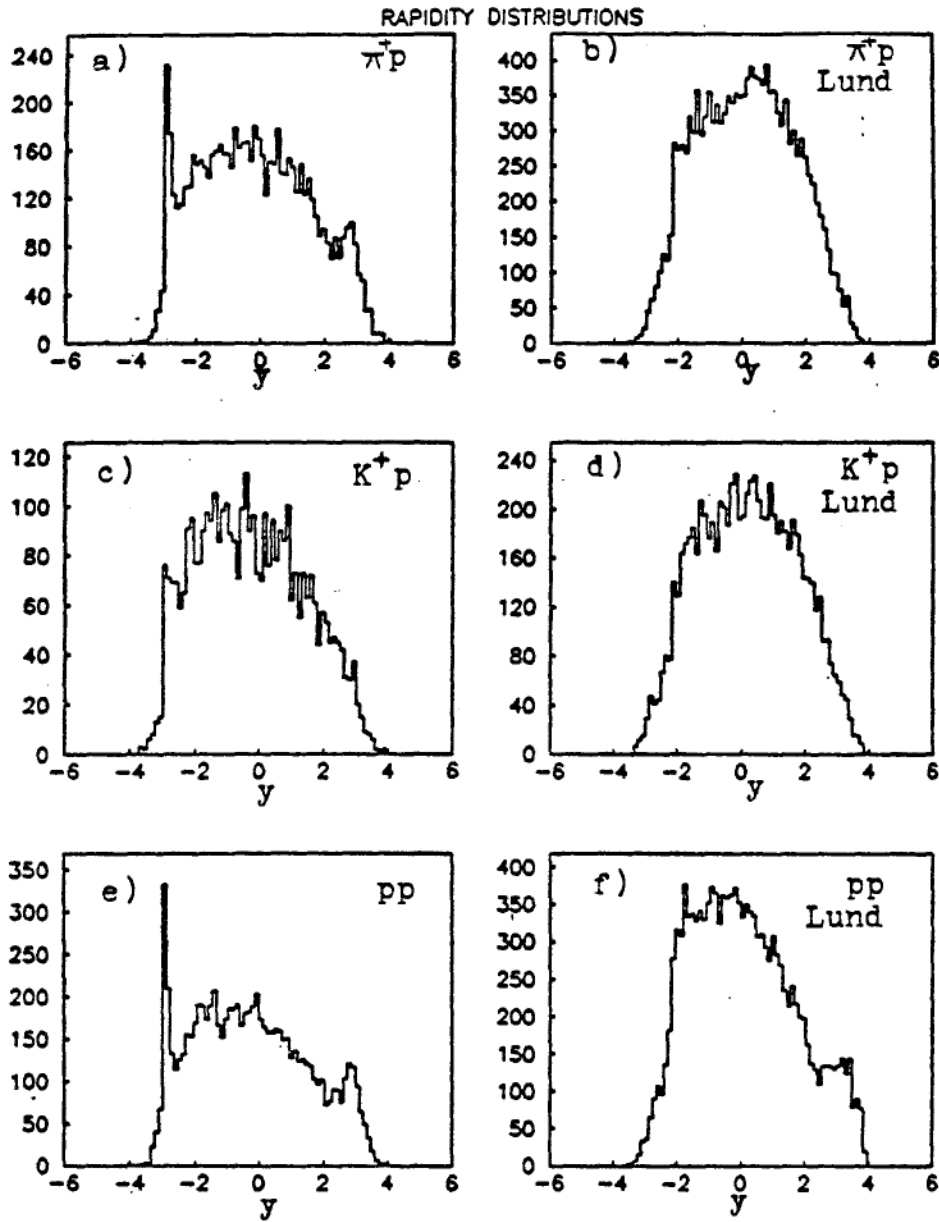


Fig. 31. Rapidity distributions for all the secondaries.